NASA Technical Paper 3484

Comparison of Several Numerical Methods for Simulation of Compressible Shear Layers

Christopher A. Kennedy and Mark H. Carpenter

December 1997

NASA Technical Paper 3484

Comparison of Several Numerical Methods for Simulation of Compressible Shear Layers

Christopher A. Kennedy
University of California • San Diego, California

Mark H. Carpenter
Langley Research Center • Hampton, Virginia

National Aeronautics and Space Administration
Langley Research Center • Hampton, Virginia 23681-2199

December 1997

Acknowledgments

The authors would like to thank B. A. Singer, C. L. Rumsey, K. R. Meadows, R. D. Joslin, D. H. Rudy, V. W. Taylor, and T. B. Gatski for their input to this report. Derivation of sixth- and eighth-order boundary conditions would not have been possible without the use of the Cray Y-MP C-90 computer at the Langley Research Center. The first author acknowledges the support of the Langley Research Center under NASA grant NAG1-1193.

Available electronically at the following URL address: http://techreports.larc.nasa.gov/ltrs/ltrs.html

Printed copies available from the following:

NASA Center for AeroSpace Information
800 Elkridge Landing Road
Linthicum Heights, MD 21090-2934
(301) 621-0390

National Technical Information Service (NTIS)
5285 Port Royal Road
Springfield, VA 22161-2171
(703) 487-4650

Contents

Summary . . . 1
Introduction . . . 1
Numerical Method . . . 2
  Extended MacCormack Schemes . . . 5
  RKLW Schemes . . . 7
  Runge-Kutta Schemes . . . 9
Formal Accuracy . . . 10
Numerical Boundary Conditions . . . 12
Filters . . . 16
Results . . . 17
Concluding Remarks . . . 19
Appendix A—Derivation of General Stencils . . . 21
Appendix B—Low-Storage Runge-Kutta Methods . . . 25
Appendix C—Nonlinear Analysis . . . 28
Appendix D—Higher Order Boundary Treatments . . . 35
Appendix E—Explicit Finite-Difference Filters . . . 38
References . . . 41
Definitions of Symbols Used in Tables . . . 44
Tables . . . 45
Figures . . . 52

Summary

An investigation is conducted of several numerical schemes for use in the computation of two-dimensional, spatially evolving, laminar, variable-density compressible shear layers. Schemes with various temporal accuracies and arbitrary spatial accuracy for both inviscid and viscous terms are presented and analyzed. All integration schemes use explicit or compact finite-difference derivative operators. Three classes of schemes are considered: an extension of MacCormack's original second-order temporally accurate method, a third-order temporally accurate variant of the coupled space-time schemes proposed by Rusanov and by Kutler, Lomax, and Warming (RKLW), and third- and fourth-order Runge-Kutta (RK) schemes. The RKLW scheme offers the simplicity and robustness of the MacCormack schemes and gives the stability domain and the nonlinear third-order temporal accuracy of the Runge-Kutta method. In each scheme, stability and formal accuracy is considered for the interior operators on the convection-diffusion equation $U_t + aU_x = \alpha_v U_{xx}$, for which a and α_v are constant. Both spatial and temporal accuracies are verified by the equation $U_t = [b(x)U_x]_x$ as well as $U_t + F_x = 0$. Numerical boundary treatments of various orders of accuracy are chosen and evaluated for asymptotic stability. Formally accurate boundary conditions are derived for explicit sixth-order; pentadiagonal sixth-order; and explicit, tridiagonal, and pentadiagonal eighth-order central-difference operators when used in conjunction with Runge-Kutta integrators. Damping of high wave-number, nonphysical data is accomplished for all schemes with explicit filters, derived to tenth order on the boundaries and twentieth order in the interior. Several schemes are used to compute variable-density compressible shear layers, where regions of large gradients of flow-field variables arise near and away from the shear-layer centerline. Results indicate that in the present simulations, the effects of differences in temporal and spatial accuracies between the schemes are less important than the filtering effects. Extended MacCormack schemes are robust but inefficient because of restrictive Courant-Friedrichs-Levy (CFL) limits. The third-order temporally accurate RKLW schemes are less dissipative but have shorter run times. The Runge-Kutta integrators did not have sufficient dissipation to be useful candidates for the computation of variable-density compressible shear layers at the levels of resolution used in the current work.

Introduction

The numerical simulation of spatially evolving, compressible shear layers has become popular as a tool to understand the mixing mechanisms involved in supersonic combustion. Simulations may involve not only the effect of compressibility but also the presence of large gradients in density caused by disparate-mass gas mixtures or large temperature gradients that arise from exothermic chemical reactions. In disparate-mass gas mixtures, the Schmidt and Lewis numbers are nonunity—usually greater than 1 in one stream and less than 1 in the other. Self-similar solutions to the laminar shear layer suggest that this nonunity gives rise to different profiles for species and temperatures relative to the velocity profile. In hydrogen-nitrogen mixing layers, vorticity occurs predominately in the low-density stream. (See ref. 1.) This phenomenon is experimentally observed in turbulent, disparate-mass supersonic shear layers. (See ref. 2.)

Computation of compressible shear layers has been largely confined to gas streams that are uniform in composition; also, the specific numerical method chosen has varied considerably. Soetrisno et al. (ref. 3) use a second-order accurate, finite-difference, total variation diminishing (TVD) scheme coupled with a second-order accurate Runge-Kutta method to study two-dimensional, temporally evolving, inviscid shear layers. Yamamoto and Daiguji (ref. 4) use either a fifth-order upwind TVD or a fourth-order monotonic upwind-centered scheme for conservation laws (MUSCL) TVD scheme, coupled with a Crank-Nicolson time integrator. Shu et al. (ref. 5) use various order, essentially nonoscillatory (ENO) finite-difference schemes, as well as compact central-difference stencils and a third-order low-storage Runge-Kutta method on a three-dimensional shear layer. The ENO schemes are particularly useful for flows in which steep gradients are present. Grinstein and Kailasanath (ref. 6) use a flux-corrected transport (FCT) algorithm to investigate three-dimensional and chemical-reaction effects. Another method that has been useful in the simulation of compressible flows is upwind biased differencing. Rai and Moin (ref. 7) use mildly dissipative fifth-order upwind differences on inviscid terms and fourth-order differences on viscous terms together

with an implicit time integration to simulate transition and turbulence in supersonic boundary layers. In a different approach to adding dissipation, Mukunda et al. (ref. 8) use the (2-4) scheme proposed by Gottlieb and Turkel (ref. 9), which is second-order accurate in time and fourth-order accurate in space, as well as the compact (2-4) version of the MacCormack (ref. 10) method developed by Carpenter (ref. 11) to study spatially evolving compressible shear layers. Lele (ref. 12) chooses a sixth-order compact central-difference stencil for viscous and inviscid terms and a third-order low-storage Runge-Kutta method to calculate temporally and spatially evolving, two-dimensional compressible shear layers. Dissipation is added by the use of implicit filters. (See ref. 13.) In a combination of compact finite-difference and Fourier spectral methods, Sandham and Reynolds (ref. 14) investigate the transition of a compressible shear layer; Guillard, Malé, and Peyret (ref. 15) use a fully spectral scheme.

Computations may be divided into two broad categories—spatial and temporal simulations. Temporal simulations allow the use of periodic numerical and physical boundary conditions in the streamwise direction, which greatly simplifies the computations. Unfortunately, they are an idealization of real shear layers. Spatial simulations require specification of both physical and numerical boundary conditions. Recently, Carpenter, Gottlieb, and Abarbanel (ref. 16) have determined numerical boundary treatments that preserve the accuracy of compact, tridiagonal sixth-order interior schemes on the model hyperbolic equation $U_t + aU_x = 0$. These treatments are also asymptotically stable with respect to time. Prior to the work of Carpenter, researchers using the sixth-order tridiagonal stencil for the interior scheme closed it at the boundaries so that the formal accuracy of the overall method was reduced.

Another relevant issue in the computation of compressible shear layers is numerical dissipation. In simulations where not all the relevant length and/or time scales of the problem are being resolved, dissipation must be added to ensure computational stability. Some numerical dissipation is desirable to remove spurious high-frequency information regardless of whether second-order derivatives are taken once with a second-order derivative operator or twice with a first-order derivative operator. The source of this high-frequency information may be intrinsic instability in the scheme, the misspecification of physical boundary conditions, the "odd-even" decoupling between grid points, or insufficient resolution (temporal and spatial). To address this problem, some researchers have resorted to implicit (ref. 13) and explicit filters (refs. 17, 18, and 19). In the present work we use explicit filters.

The goal of the present study is to generate families of schemes with arbitrarily high spatial accuracy for both viscous and inviscid terms, coupled with explicit time integrations from second to fourth order. Schemes are applied to highly resolved, spatially evolving, compressible shear-layer calculations devoid of discontinuities. The accuracy, stability, and robustness of the schemes are considered with particular attention to compressible, variable-density, nonreacting flows. Analyses of both compact and explicit interior schemes have been provided, as well as a variety of choices for boundary closures and explicit filters. Stability is considered not only through Von Neumann analysis but also through matrix analysis of various boundary and interior treatments. The schemes examined are the following: extended MacCormack-type schemes, a new variant of the schemes presented by Rusanov (ref. 20) and by Kutler, Lomax, and Warming (refs. 21, 22, and 23) (RKLW), and Runge-Kutta (RK) schemes.

Numerical Method

The governing equations are solved in conservative form with the SPARK2D (ref. 24) code and may be written as

$$\frac{\partial \mathbf{U}}{\partial t} + \frac{\partial \mathbf{F}(\mathbf{U})}{\partial x} + \frac{\partial \mathbf{G}(\mathbf{U})}{\partial y} = \mathbf{H} \tag{1}$$

where

$$\left.\begin{aligned}
\mathbf{U} &= \begin{bmatrix} \rho \\ \rho u \\ \rho v \\ \rho e_0 \\ \rho Y_i \end{bmatrix} \quad \mathbf{F} = \begin{bmatrix} \rho u \\ \rho u u - \sigma_{xx} \\ \rho u v - \sigma_{yx} \\ (\rho e_0 - \sigma_{xx}) u - \sigma_{xy} v + \mathbf{q}_x \\ \rho u Y_i + \rho \tilde{u}_i Y_i \end{bmatrix} \\
\mathbf{G} &= \begin{bmatrix} \rho v \\ \rho u v - \sigma_{xy} \\ \rho v v - \sigma_{yy} \\ (\rho e_0 - \sigma_{yy}) v - \sigma_{yx} u + \mathbf{q}_y \\ \rho v Y_i + \rho \tilde{v}_i Y_i \end{bmatrix} \quad \mathbf{H} = \begin{bmatrix} 0 \\ 0 \\ 0 \\ 0 \\ 0 \end{bmatrix}
\end{aligned}\right\} \tag{2}$$

ρ is the density; u is the streamwise velocity; v is the transverse velocity; $\sigma_{\beta\alpha}$ is the Newtonian stress tensor; e_0 is the total internal energy; $\mathbf{q}_\alpha$ is the heat flux vector; Y_i is the species mass fraction; and $\tilde{u}_i$ and $\tilde{v}_i$ are streamwise and transverse components of the diffusion velocity, respectively. Roman indicies (e.g., i) correspond to the species index, whereas Greek ones (e.g., α) correspond to spatial indicies. Throughout this text, the inviscid derivative operators are those used to differentiate $\mathbf{F}$ and $\mathbf{G}$, whereas viscous derivatives are those used to generate derivative terms in the expressions for the stress tensor, heat flux vector, and diffusion velocity.

In the finite-difference schemes considered here, for constant grid spacing Δx, the spatial derivative of a function f ($f' = f_x$), is given in matrix form as

$$\left.\begin{aligned}
\mathbf{P} f_x &= \frac{1}{\Delta x} \mathbf{Q} f \\
f_x &= \frac{1}{\Delta x} \mathbf{P}^{-1} \mathbf{Q} \\
f &= \frac{1}{\Delta x} \mathbf{A} f
\end{aligned}\right\} \tag{3}$$

To avoid the increased operation count necessary to invert large bandwidth matrices, the bandwidth of the matrix $\mathbf{P}$ is not considered operationally to be larger than pentadiagonal. Determination of the specific centered-difference stencil is accomplished by writing

$$\begin{aligned}
\cdots + \beta f'_{i-2} + \alpha f'_{i-1} + f'_i + \alpha f'_{i+1} + \beta f'_{i+2} + \cdots = a &\frac{f_{i+1} - f_{i-1}}{\Delta x} \\
+ b &\frac{f_{i+2} - f_{i-2}}{\Delta x} \\
+ c &\frac{f_{i+3} - f_{i-3}}{\Delta x} \\
+ \cdots &
\end{aligned} \tag{4}$$

where the coefficients $\alpha, \beta, \cdots$ form the matrix $\mathbf{P}$; $a, b, \cdots$ form the matrix $\mathbf{Q}$; and f_i and f'_i are the values of some function and its derivative at grid point i, respectively. By defining the Fourier transform and the inverse Fourier transform of the discrete function value f_m with (ref. 25)

$$f_m = \frac{1}{\sqrt{2\pi}} \int_{-\pi}^{\pi} e^{im\xi} \, \hat{f}(\xi) \, d\xi \tag{5}$$

$$\hat{f}(\xi) = \frac{1}{\sqrt{2\pi}} \sum_{m=-\infty}^{\infty} e^{-im\xi} \, f_m \tag{6}$$

where ξ is the Fourier dual variable; if $\Psi(\xi)$ is the approximation of the derivative of f in Fourier space or the Fourier image of $f^{'}$, $f^{'}_m$ is given in Fourier space as

$$f^{'}_m = \frac{1}{\sqrt{2\pi}\,(\Delta x)} \int_{-\pi}^{\pi} e^{im\xi}\ \Psi(\xi)\ \widehat{f}(\xi)\ d\xi \tag{7}$$

The finite-difference stencil given in equation (4) becomes

$$\begin{aligned} &\frac{1}{\sqrt{2\pi}} \int_{-\pi}^{\pi} \left[\left(\cdots + \beta\ e^{-2i\xi} + \alpha\ e^{-i\xi} + 1 + \alpha\ e^{i\xi}\ + \beta\ e^{2i\xi} + \cdots \right) \Psi(\xi)\ \widehat{f}(\xi)\ d\xi \right] \\ &= \frac{1}{\sqrt{2\pi}} \int_{-\pi}^{\pi} \left[\left(\cdots - c\ e^{-3i\xi} - b\ e^{-2i\xi} - a\ e^{-i\xi} + a\ e^{i\xi} + b\ e^{2i\xi} + c\ e^{3i\xi} + \cdots \right) \widehat{f}(\xi)\ d\xi \right] \end{aligned} \tag{8}$$

Consequently,

$$\Psi = \frac{i\,[2a\ \sin(\xi)\ +\ 2b\ \sin(2\xi)\ +\ 2c\ \sin(3\xi)\ +\ \cdots]}{[1\ +\ 2\alpha\ \cos(\xi)\ +\ 2\beta\ \cos(2\xi)\ +\ \cdots]} \tag{9}$$

With the spectral representation of $f(x)$ written as

$$f(x) = \frac{1}{\sqrt{2\pi}} \int_{-\infty}^{\infty} e^{i\omega x}\ \widehat{f}(\omega)\ d\omega \tag{10}$$

it can be seen that $f^{'}(x)$ in Fourier space has the form

$$f^{'}(x) = i\omega\ \widehat{f}(\omega) \tag{11}$$

If the Fourier image of the finite-difference derivative operator is expanded in a Taylor series in ξ, coefficients of the stencil can be chosen to approximate the spectral derivative to some desired accuracy (i.e., $\Psi \approx i\xi$).

For an arbitrarily skewed stencil, the stencil and its Fourier image are given by

$$\begin{aligned} \cdots\ +\ \beta_L f^{'}_{i-2}\ +\ \alpha_L f^{'}_{i-1}\ +\ f^{'}_i\ +\ \alpha_R f^{'}_{i+1}\ +\ \beta_R f^{'}_{i+2}\ +\ \cdots\ = \ & \frac{\Upsilon f_i}{\Delta x} \\ & + \frac{a_L f_{i-1}\ +\ a_R f_{i+1}}{\Delta x} \\ & + \frac{b_L f_{i-2}\ +\ b_R f_{i+2}}{\Delta x} \\ & + \frac{c_L f_{i-3}\ +\ c_R f_{i+3}}{\Delta x} \\ & + \cdots \end{aligned} \tag{12}$$

and

$$\Psi = \frac{\left\{ \begin{array}{c} [\Upsilon + (a_R + a_L)\ \cos(\xi) + (b_R + b_L)\ \cos(2\xi) + (c_R + c_L)\ \cos(3\xi) + \cdots] \\ +\ i[(a_R - a_L)\ \sin(\xi) + (b_R - b_L)\ \sin(2\xi) + (c_R - c_L)\ \sin(3\xi) + \cdots] \end{array} \right\}}{\left\{ \begin{array}{c} [1 + (\alpha_R + \alpha_L)\ \cos(\xi) + (\beta_R + \beta_L)\ \cos(2\xi) + \cdots] \\ +\ i[(\alpha_R - \alpha_L)\ \sin(\xi) + (\beta_R - \beta_L)\ \sin(2\xi) + \cdots] \end{array} \right\}} \tag{13}$$

where the subscripts L and R are used to denote left and right.

Finally, for predictor-corrector dissipative schemes (ref. 16), we have

$$\begin{aligned}\cdots + \beta f'_{i-2} + \alpha f'_{i-1} + f'_i + \alpha f'_{i+1} + \beta f'_{i+2} + \cdots = & \frac{G f_i}{\Delta x} \\ & \pm \frac{(B \mp A) f_{i-1} + (B \pm A) f_{i+1}}{\Delta x} \\ & \pm \frac{(D \mp C) f_{i-2} + (D \pm C) f_{i+2}}{\Delta x} \\ & \pm \frac{(F \mp E) f_{i-3} + (F \pm E) f_{i+3}}{\Delta x} \\ & \pm \cdots \end{aligned} \tag{14}$$

and

$$\Psi = \frac{\left\{ \begin{array}{c} \{\pm 2B[\cos(\xi) - 1] \pm 2D[\cos(2\xi) - 1] \pm 2F[\cos(3\xi) - 1] \pm \cdots\} \\ + i[2A \sin(\xi) + 2C \sin(2\xi) + 2E \sin(3\xi) + \cdots] \end{array} \right\}}{[1 + 2\alpha \cos(\xi) + 2\beta \cos(2\xi) + \cdots]} \tag{15}$$

The predictor-corrector stencils become centered stencils for $B = D = F = G = 0$. All second derivatives are taken effectively by successively applying a first derivative operator twice. A consequence of this application is that the wave number $\xi = \pi$ becomes neutrally stable for central difference schemes and may cause a loss of stability on nonlinear problems. This wave number is sometimes referred to as the "π" mode.

When predictor-corrector finite-difference schemes are used, viscous derivatives are calculated with explicit stencils (i.e., $\mathbf{P} = \mathbf{I}$, where $\mathbf{I}$ is the identity matrix, and $\mathbf{Q} = \mathbf{A}$). An explicit stencil of $(N-1)$th-order accuracy is used for the evaluation of viscous terms in the schemes when the derivatives of $\mathbf{F}$ and $\mathbf{G}$ are calculated to Nth-order accuracy. Runge-Kutta schemes use the same derivative operator for both viscous and inviscid derivatives. Further discussion of the derivation of the stencils is contained in appendix A.

Extended MacCormack Schemes

In 1969, MacCormack (ref. 10) introduced a two-stage numerical scheme for compressible flows with a predictor stage followed by a corrector stage. The scheme is second-order accurate in both space and time and is widely applicable, in part, because of its simplicity and robustness. Details of the method can be found in many places (refs. 26 to 29). Attempts made by Gottlieb and Turkel (ref. 9) to improve the method increased the inviscid spatial accuracy to fourth order. This scheme has been popular among researchers involved with highly resolved flow fields. (See refs. 30, 31, 32, and 8.) Carpenter (ref. 11) further modified this scheme by using a compact fourth-order inviscid stencil with a third-order upwind viscous stencil. The scheme was slightly more accurate than the Gottlieb-Turkel scheme. Bayliss (ref. 33) extended the Gottlieb-Turkel scheme to sixth-order accuracy for the inviscid terms.

Extended MacCormack schemes take the original MacCormack scheme to arbitrary spatial accuracy in both the inviscid and viscous terms. These schemes are obtained by using the skewed stencils (eq. (12)) to generate viscous terms in the vectors $\mathbf{F}$ and $\mathbf{G}$, and the predictor-corrector stencils (eq. (14)) are used to evaluate the derivatives of $\mathbf{F}$ and $\mathbf{G}$. Symbolically, the schemes may be represented for the equation

$$U_t + F_x = 0 \tag{16}$$

as

$$\left. \begin{aligned} U_i^* &= U_i^n - \lambda \Delta^+ F^n \\ U_i^{**} &= U_i^* - \lambda \Delta^- F^* \\ U_i^{n+1} &= \frac{1}{2}(U_i^n + U_i^{**}) \end{aligned} \right\} \tag{17}$$

where Δ^+ and Δ^- are the forward and backward difference operators and $\lambda = \frac{\Delta t}{\Delta x}$ is the Courant-Friedrichs-Levy (CFL) number.

The stability of the extended MacCormack schemes may be conveniently analyzed in Fourier space with conventional Von Neumann analysis on the convection-diffusion equation $U_t + aU_x = \alpha_v U_{xx}$ with a and α_v as constants. If Ψ and $-\Psi^\star$ (where $\Psi^\star$ is the complex conjugate of Ψ) are defined as the Fourier images of Δ^+ and Δ^-, Ψ_v and $-\Psi_v^\star$ are defined as the Fourier images of Δ_v^+ and Δ_v^-, the viscous derivatives; $\widehat{U}$ is defined as the Fourier transform of U^n; $\lambda' = \frac{a\Delta t}{\Delta x}$; $\lambda_v = \frac{\alpha_v \Delta t}{(\Delta x)^2}$ is the viscous CFL number or diffusion number; and $G \equiv \frac{\widehat{U}^{n+1}}{\widehat{U}^n}$ is the amplification factor, then these schemes can be written as

$$\left.\begin{aligned} \frac{\widehat{U}^*}{\widehat{U}^n} &= 1 - \lambda'\Psi - \lambda_v \Psi\Psi_v^\star \\ \frac{\widehat{U}^{**}}{\widehat{U}^*} &= 1 + \lambda'\Psi^\star - \lambda_v \Psi^\star\Psi_v \\ G &= \frac{1}{2}\left(1 + \frac{\widehat{U}^{**}}{\widehat{U}^*}\frac{\widehat{U}^*}{\widehat{U}^n}\right) \end{aligned}\right\} \tag{18}$$

The amplification factor G represents the magnitude of the amplification of a given frequency when the solution is advanced one time step. Use of the letter G here should not be confused with its use in defining the dissipative stencils. To determine the maximum CFL number, G may be analyzed for the interior scheme or the amplification matrix $\mathbf{G}$ may be considered for the full scheme with boundary points. For $-\pi \le \xi < \pi$, the magnitude of G must never exceed 1, or the spectral radius of $\mathbf{G}$ must be less than or equal to 1; this is required for stability. For the convection-diffusion equation $U_t + aU_x = \alpha_v U_{xx}$, the amplification factor and matrix are written as

$$|G| = \left|\frac{1}{2}\left[1 + \left(1 + \lambda'\Psi^\star - \lambda_v\Psi^\star\Psi_v\right)\left(1 - \lambda'\Psi - \lambda_v\Psi\Psi_v^\star\right)\right]\right| \tag{19}$$

$$\mathbf{G} = \frac{1}{2}\left[\mathbf{I} + \left(\mathbf{I} - \lambda'\mathbf{A}^- + \lambda_v\mathbf{A}^-\mathbf{A}_v^+\right)\left(\mathbf{I} - \lambda'\mathbf{A}^+ + \lambda_v\mathbf{A}^+\mathbf{A}_v^-\right)\right] \tag{20}$$

where $\mathbf{A}^+$ and $\mathbf{A}^-$ are the forward and backward inviscid matrix derivative operators and $\mathbf{A}_v^+$ and $\mathbf{A}_v^-$ are the forward and backward matrix operators for the viscous derivatives.

For consistency, the explicit coefficients must sum to zero as follows:

$$(F - E) + (D - C) + (B - A) + G + (B + A) + (D + C) + (F + E) = 0 \tag{21}$$

or $G = -2(B + D + F)$. Values of B, D, and F may be selected on the basis of their effect on the dispersion, dissipation, and CFL numbers of the scheme. We have chosen to maximize the inviscid CFL number and retain the largest viscous CFL limit possible. The coefficients A, C, E, α, and β are chosen to satisfy the accuracy requirement of the stencil.

Table 1 lists the coefficients of the extended MacCormack predictor-corrector stencils and the maximum CFL number $\lambda_{\max}$ for the inviscid problem ($\alpha_v = 0$) in the absence of boundaries. The letters E, T, and P indicate that the matrix $\mathbf{P}$ is either diagonal/explicit, tridiagonal, or pentadiagonal, respectively. The notation (2-6E) should be interpreted as second-order temporal accuracy with sixth-order spatial accuracy for both the inviscid and viscous terms; the letter E indicates that the inviscid derivative operator is explicit. Some confusion may arise because many schemes found in the literature do not treat viscous terms at all and others do not retain the stated inviscid accuracy on viscous terms.

Figure 1 presents the stability boundary of these schemes as a function of the viscous and inviscid CFL numbers, again in the absence of boundaries. Regions in the lower left portion of the figure represent the stable region, whereas regions in the upper right portion are unstable. While optimizing these schemes it was noticed that contours of the stability boundary can be dramatically altered by different choices of B, D, and F. Optimizing was done by simply scanning parameter space for combinations with desirable stability characteristics. Each scheme can be considered as optimized, although a 5-percent improvement may be possible. Care should be exercised in optimizing the "flipping" parameters B, D, and F because many of the combinations share the maximum inviscid CFL limit of the scheme yet very few of this subset have a boundary $G = 1$ that does not intersect the origin. The (2-8T) scheme was found to have no values of B, D, and F for which the boundary $G = 1$ did not intersect the origin. In many flow fields of interest, the local viscous and inviscid CFL numbers are likely to lie outside the stability domain in the (2-8T) scheme. Explicit schemes possess significantly larger stability domains than their compact counterparts because of the increased truncation error of the explicit derivative operator. Thus, the CFL limits for compact schemes are more severe than those for multidimensional schemes. (See refs. 10 and 9.)

Note that the (2-4E) scheme differs from that proposed by Gottlieb and Turkel (ref. 9) where $B = -A$ and $D = -C$. If used with the explicit third-order accurate viscous derivative, the Gottlieb-Turkel scheme has a viscous CFL limit of zero as CFL $\rightarrow 0$. MacCormack's original scheme, (2-2E), is included in table 1 and figure 1 for completeness. The explicit skewed viscous stencils ($\beta_L = \alpha_L = \alpha_R = \beta_R = 0$) are given in table 2.

RKLW Schemes

Rusanov (ref. 20) derived a finite-difference scheme for nonlinear hyperbolic systems that was uniformly third-order accurate in space and time. This scheme was considered for use in the computation of discontinuous solutions. Three spatial difference operators were used in its construction—mean value, difference, and identity. These operators were combined with a three-stage, third-order Runge-Kutta method. Later, Burstein and Mirin (ref. 34) derived a similar method. Because function evaluations needed to be made on a staggered mesh, Kutler, Lomax, and Warming (refs. 21, 22, and 23) adapted Rusanov's scheme by replacing the first two stages with MacCormack's scheme. Hereinafter, this scheme is referred to as RKLW. This adaptation made the programming logic simpler and facilitated the inclusion of a source term and the extension to multidimensions. Various investigators have applied this scheme to both high-speed flow (ref. 35) and to meteorological flows (refs. 36, 37, and 38). Further discussion of the RKLW schemes can be found in the textbook by Anderson, Tannehill, and Pletcher (ref. 26) and in two papers by Yanenko et al. (refs. 28 and 29). Attempts to proceed to uniformly fourth-order schemes for hyperbolic equations (refs. 39, 40, and 41) have been successful, but have not been used extensively, probably because of their enormous complexity.

The proposed RKLW method is a generalization of the third-order predictor-corrector format of Kutler, Lomax, and Warming (refs. 21, 22, and 23) to arbitrary spatial accuracy in both viscous and inviscid terms within the temporally third-order Runge-Kutta (RK) accuracy constraints. The implementation of this scheme for the equation $U_t + F_x = 0$ is solved numerically as

$$\left.\begin{aligned} U_i^* &= U_i^n - \beta_1 \lambda \Delta^+ F^n \\ U_i^{**} &= U_i^* - \beta_1 \lambda \Delta^- F^* \\ U_i^{\#} &= (1-\beta_2) U_i^n + \beta_2 U_i^{**} \\ U_i^{n+1} &= \frac{1}{3}\left[U_i^n + 2(U_i^{\#} - \lambda \Delta^c) F^{\#}\right] \end{aligned}\right\} \tag{22}$$

where Δ^c is the central-difference operator and the forward and backward differencing operators are the same as those used in the extended MacCormack schemes. The values of β_1 and β_2 are 1 and 1/4, respectively. The two degrees of freedom inherent in the general three-stage, third-order Runge-Kutta formulation (ref. 42) are used to accommodate symmetric ($\alpha_{31} = \alpha_{32}$ in eq. (23)), predictor-corrector spatial differencing.

The traditional Runge-Kutta scheme may be represented for the equation $U_t = -F_x = -F_U U_x = -fU_x$ as

$$\left.\begin{aligned} U^* &= U^n - a_{21}\lambda f^n \mathbf{A}_1 U^n \\ U^{**} &= U^n - a_{31}\lambda f^n \mathbf{A}_1 U^n - a_{32}\lambda f^* \mathbf{A}_2 U^* \\ U^{n+1} &= U^n - b_1\lambda f^n \mathbf{A}_1 U^n - b_2\lambda f^* \mathbf{A}_2 U^* - b_3\lambda f^{**} \mathbf{A}_3 U^{**} \end{aligned}\right\} \tag{23}$$

where the subscript associated with the matrix operator $\mathbf{A}$ represents the finite difference operator used on the relevant stage—forward, backward, or centered.

Runge-Kutta schemes are often described in terms of the Butcher array. (See ref. 42.) The Butcher array for the present scheme is given as

$$\begin{array}{c|ccc} 0 & & & \\ c_2 & a_{21} & & \\ c_3 & a_{31} & a_{32} & \\ \hline & b_1 & b_2 & b_3 \end{array} = \begin{array}{c|ccc} 0 & & & \\ 1 & & & \\ \frac{1}{2} & \frac{1}{4} & \frac{1}{4} & \\ \hline & \frac{1}{6} & \frac{1}{6} & \frac{2}{3} \end{array} \tag{24}$$

Hence, $\beta_1 = \alpha_{21}$ and $\beta_2 = \alpha_{31} = \alpha_{32}$. Symbols (letters) used for terms contained in the Butcher array should not be confused with those symbols (letters) involved in the definition of the finite-difference coefficients. Values of c_i correspond to the time at which the ith stage is evaluated, that is, zero being the nth stage and one being the $(n+1)$th stage.

The stability of the scheme is considered in Fourier space in the linear model equation $U_t + aU_x = \alpha_v U_{xx}$ as

$$\left.\begin{aligned} \frac{\widehat{U}^*}{\widehat{U}^n} &= 1 - \beta_1\lambda'\Psi - \beta_1\lambda_v\Psi\Psi_v^\star \\ \frac{\widehat{U}^{**}}{\widehat{U}^*} &= 1 + \beta_1\lambda'\Psi^\star - \beta_1\lambda_v\Psi^\star\Psi_v \\ \frac{\widehat{U}^{\#}}{\widehat{U}^n} &= 1 + \beta_2\left(\frac{\widehat{U}^{**}}{\widehat{U}^n} - 1\right) \\ \frac{\widehat{U}^{n+1}}{\widehat{U}^n} &= \frac{1}{3}\left[1 + 2(1 - \lambda'\Psi^c + \lambda_v\Psi^c\Psi^c)\frac{\widehat{U}^{\#}}{\widehat{U}^n}\right] \end{aligned}\right\} \tag{25}$$

where Ψ^c is the Fourier image of the central-difference stencil. For the final stage of this method, the dissipative difference operator is used as a central-difference operator by setting $B = D = F = 0$. The optimum values of B, D, and F are different from those of the extended MacCormack schemes. They have been chosen to maximize the size of the stability envelope under the constraint that $|G| \leq 1$ or that the spectral radius of $\mathbf{G}$ is less than or equal to 1, where

$$
\begin{aligned}
G = & \frac{1}{3} + \frac{2}{3}(1 - \lambda' \Psi^c + \lambda_v \Psi^c \Psi^c) \\
& \times \left\{ 1 + \beta_2 \left[\left(1 + \beta_1 \lambda' \Psi^\star - \beta_1 \lambda_v \Psi^\star \Psi_v \right) \left(1 - \beta_1 \lambda' \Psi - \beta_1 \lambda_v \Psi \Psi_v^\star \right) - 1 \right] \right\} \qquad (26) \\
\mathbf{G} = & \frac{1}{3}\mathbf{I} + \frac{2}{3}(\mathbf{I} - \lambda' \mathbf{A}^c + \lambda_v \mathbf{A}^c \mathbf{A}^c) \\
& \times \left\{ \mathbf{I} + \beta_2 \left[\left(\mathbf{I} - \beta_1 \lambda' \mathbf{A}^- + \beta_1 \lambda_v \mathbf{A}^- \mathbf{A}_v^+ \right) \left(\mathbf{I} - \beta_1 \lambda' \mathbf{A}^+ + \beta_1 \lambda_v \mathbf{A}^+ \mathbf{A}_v^- \right) - \mathbf{I} \right] \right\} \qquad (27)
\end{aligned}
$$

Table 3 summarizes the RKLW schemes. Viscous stencils are the same as those used in the extended MacCormack schemes. (See table 2.) Figure 2 presents the stability boundary of these schemes in the absence of boundaries. As for the extended MacCormack schemes, explicit schemes have less restrictive CFL bounds than the compact schemes with the same spatial order of accuracy, and increasing the order of accuracy of the spatial operator reduces the stability domain. The (3-2E) scheme is the analog of the original MacCormack scheme with the Runge-Kutta integrator. By simply setting $B = D = F = G = 0$, the RKLW scheme becomes the third-order Runge-Kutta scheme. Both RKLW and its corresponding third-order Runge-Kutta method require three storage locations (3M) as opposed to the low-storage (2M) method proposed by Williamson (ref. 43).

Runge-Kutta Schemes

A significant portion of direct numerical simulations (DNS) and well-resolved model-free simulations of compressible flows have used a Runge-Kutta method. Unlike the extended MacCormack and RKLW schemes, space and time are not coupled in the numerical method. A commonly used Runge-Kutta method is the three-stage, third-order, low-storage scheme (ref. 43). Combined with a sixth-order, compact central-difference operator, this method has been used in the simulation of compressible shear layers (ref. 12), supersonic boundary-layer transition (ref. 44), and compressible isotropic turbulence (ref. 45).

In a more traditional approach, common variants of the third- and fourth-order Runge-Kutta time-integration schemes are combined with explicit and compact differencing. The Butcher array for these is given by

$$
\begin{array}{c|ccc}
0 & & & \\
c_2 & a_{21} & & \\
c_3 & a_{31} & a_{32} & \\
\hline
 & b_1 & b_2 & b_3
\end{array}
=
\begin{array}{c|ccc}
0 & & & \\
\frac{1}{3} & \frac{1}{3} & & \\
\frac{2}{3} & 0 & \frac{2}{3} & \\
\hline
 & \frac{1}{4} & 0 & \frac{3}{4}
\end{array}
\qquad (28)
$$

for third-order temporal accuracy and by

$$
\begin{array}{c|cccc}
0 & & & & \\
c_2 & a_{21} & & & \\
c_3 & a_{31} & a_{32} & & \\
c_4 & a_{41} & a_{42} & a_{43} & \\
\hline
 & b_1 & b_2 & b_3 & b_4
\end{array}
=
\begin{array}{c|cccc}
0 & & & & \\
\frac{1}{2} & \frac{1}{2} & & & \\
\frac{1}{2} & 0 & \frac{1}{2} & & \\
1 & 0 & 0 & 1 & \\
\hline
 & \frac{1}{6} & \frac{2}{6} & \frac{2}{6} & \frac{1}{6}
\end{array}
\qquad (29)
$$

for fourth-order temporal accuracy. The application of these schemes to the equation $U_t + F_x = 0$ is

$$\left.\begin{aligned} U_i^* &= U_i^n - a_{21}\lambda\Delta^c F^n \\ U_i^{**} &= U_i^n - a_{32}\lambda\Delta^c F^* \\ U_i^{n+1} &= U_i^n + (b_1\Delta^c F_i^n + b_2\Delta^c F_i^* + b_3\Delta^c F_i^{**}) \end{aligned}\right\} \tag{30}$$

and

$$\left.\begin{aligned} U_i^* &= U_i^n - a_{21}\lambda\Delta^c F^n \\ U_i^{**} &= U_i^n - a_{32}\lambda\Delta^c F^* \\ U_i^{***} &= U_i^n - a_{43}\lambda\Delta^c F^{**} \\ U_i^{n+1} &= U_i^n + (b_1\Delta^c F_i^n + b_2\Delta^c F_i^* + b_3\Delta^c F_i^{**} + b_4\Delta^c F_i^{***}) \end{aligned}\right\} \tag{31}$$

Analysis of the stability of the Runge-Kutta schemes can be done again with the equation $U_t + aU_x = \alpha_v U_{xx}$. The amplification polynomial (ref. 42) for the linear problem is given by

$$\mathbf{G} = 1 - \left(\sum_{i=1}^{ns} b_i\right)\mathbf{Z} + \left(\sum_{i=1}^{ns} b_i c_i\right)\mathbf{Z}^2 - \left(\sum_{i,j=1}^{ns} b_i a_{ij} c_j\right)\mathbf{Z}^3 + \left(\sum_{i,j,k=1}^{ns} b_i a_{ij} a_{jk} c_k\right)\mathbf{Z}^4 + \cdots \tag{32}$$

where $\mathbf{Z}$ may be either $(\lambda'\mathbf{\Psi}^c - \lambda_v\mathbf{\Psi}^c\mathbf{\Psi}^c)$ or $(\lambda'\mathbf{A}^c - \lambda_v\mathbf{A}^c\mathbf{A}^c)$, depending on whether one is interested in amplification factor or matrix, and ns is the number of stages in the Runge-Kutta scheme. The schemes are summarized in table 4. Figures 3 and 4 show the stability boundary of the third- and fourth-order Runge-Kutta/centered-difference schemes, determined by the amplification factor. Stability appears to be significantly augmented by going to fourth-order accuracy. Figure 3 shows a characteristic of third- and fifth-order Runge-Kutta formulas: a tendency for the stability domain to become small as the viscous CFL $\rightarrow 0$. These stability domains are independent of which of the two free-parameter families of three-stage, third-order and four-stage, fourth-order Runge-Kutta schemes are chosen. All Runge-Kutta schemes considered use centered stencils to evaluate viscous derivatives. A brief discussion of low-storage Runge-Kutta schemes is contained in appendix B. The stability of Runge-Kutta schemes applied to the Navier-Stokes equations has been considered by Sowa (ref. 46) for second-order centered spatial derivatives and Runge-Kutta coefficients in which all $a_{ij} = 0$, except when $i = j + 1$. Temporal accuracy of the Runge-Kutta schemes was verified in the representative (4-8P) case. The linear equation $U_t + U_x = 0$ was solved for various CFL numbers with a sinusoidal initial and boundary condition and 75 grid points per wavelength. As table 5 shows, fourth-order temporal accuracy was recovered. Table 6 contains the error when $U_t + U_x = 0$ was solved at a CFL number of 0.01 on various grids to ensure that spatial error dominated the total error. As can be seen, eighth-order spatial accuracy was recovered. In each of these cases, machine precision becomes a factor at high resolution.

Formal Accuracy

To determine the formal spatial and temporal accuracy of the interior schemes used in this study, the amplification factor and the linear equation $U_t + aU_x = \alpha_v U_{xx}$ are used to derive the modified equation. (See refs. 26, 27, 47, and 48.)

The exact solution to the convection-diffusion equation can be solved with the continuous Fourier transform as

$$\frac{1}{\sqrt{2\pi}}\int_{-\infty}^{\infty}\left(\widehat{U}_t + ia\omega\widehat{U} + \alpha_v\omega^2\widehat{U}\right)e^{i\omega x}d\omega = 0 \tag{33}$$

or

$$\widehat{U}_t + ia\omega\widehat{U} + \alpha_v\omega^2\widehat{U} = 0 \tag{34}$$

This equation may be integrated as

$$\ln \widehat{U}\Big|_{t^n}^{t^n+\tau} = -\left(ia\omega + \alpha_v\omega^2\right) t\Big|_{t^n}^{t^n+\tau} \tag{35}$$

where t^n is the nth time step, to give

$$\widehat{U}\Big|_{t^n+\tau} = \exp\left[-\left(ia\omega + \alpha_v\omega^2\right)\tau\right] \widehat{U}\,|_{t^n} \tag{36}$$

At $\tau = (\Delta t)$, the value of the amplification factor is then

$$G_{\text{exact}} = \exp\left[-\left(ia\omega + \alpha_v\omega^2\right)(\Delta t)\right] \tag{37}$$

or, in terms of ξ,

$$G_{\text{exact}} = \exp\left[-\left(i\lambda'\xi + \lambda_v\xi^2\right)\right] \tag{38}$$

where $\lambda' = \frac{a\Delta t}{\Delta x}$ and $\lambda_v = \frac{\alpha_v \Delta t}{(\Delta x)^2}$.

The error of the numerical scheme in Fourier space can now be written as (refs. 49 and 25)

$$\frac{\ln\,(G_{\text{scheme}})}{\Delta t} - \frac{\ln\,(G_{\text{exact}})}{\Delta t} = \sum_{k=0}^{\infty} A_k (i\xi)^k \tag{39}$$

Replacing all occurrences of ξ^k with its transform $(-i\Delta x)^k \frac{\partial^k}{\partial x^k}(U_m)$ yields

$$\frac{\ln\,(G_{\text{scheme}})}{\Delta t} - \frac{\ln\,(G_{\text{exact}})}{\Delta t} = \sum_{k=0}^{\infty} A_k (\Delta x)^k \frac{\partial^k}{\partial x^k}(U_m) \tag{40}$$

A symbolic manipulator may now be used to expand $\ln G$ in a power series and to solve for A_k.

The modified equation of several representative schemes is now presented. Because the resulting expressions are of excessive length, only fourth-order tridiagonal schemes are considered. The modified equation for the (2-4T) scheme is given as

$$\begin{aligned}
\frac{\partial U}{\partial t} + a\frac{\partial U}{\partial x} - \alpha_v \frac{\partial^2 U}{\partial x^2} = {} & \frac{a^3}{6}(\Delta t)^2 \frac{\partial^3 U}{\partial x^3} \\
& + \frac{a^2}{72}\left[9a^2(\Delta t)^3 - 36\alpha_v(\Delta t)^2 - 16B^2(\Delta x)^2(\Delta t)\right]\frac{\partial^4 U}{\partial x^4} \\
& + \frac{a}{180}\left[90\alpha_v^2(\Delta t)^2 - 90a^2\alpha_v(\Delta t)^3 + 9a^4(\Delta t)^4 + 80\alpha_v B^2(\Delta x)^2(\Delta t)\right]\frac{\partial^5 U}{\partial x^5} \\
& + \frac{a}{180}\left[-40a^2B^2(\Delta x)^2(\Delta t)^2 + (\Delta x)^4\right]\frac{\partial^5 U}{\partial x^5} \\
& + O\left[(\Delta x)^5\right]
\end{aligned} \tag{41}$$

and for the (3-4T) RKLW scheme as

$$\frac{\partial U}{\partial t} + a\frac{\partial U}{\partial x} - \alpha_v \frac{\partial^2 U}{\partial x^2} = -\frac{a^2}{216}\left[9a^2(\Delta t)^3 + 16B^2(\Delta x)^2(\Delta t)\right]\frac{\partial^4 U}{\partial x^4}$$
$$+ \frac{a}{540}\left[90a^2\alpha_v(\Delta t)^3 - 18a^4(\Delta t)^4 + 80\alpha_v B^2(\Delta x)^2(\Delta t) + 3(\Delta x)^4\right]\frac{\partial^5 U}{\partial x^5}$$
$$+ O\left[(\Delta x)^5\right] \tag{42}$$

The term $(\Delta x)^2(\Delta t)$ represents the dominant space-time error term for both the extended MacCormack and RKLW schemes. For the (3-4T) and (4-4T) Runge-Kutta schemes,

$$\frac{\partial U}{\partial t} + a\frac{\partial U}{\partial x} - \alpha_v \frac{\partial^2 U}{\partial x^2} = -\frac{a^4}{24}(\Delta t)^3\frac{\partial^4 U}{\partial x^4}$$
$$+ \frac{a}{180}\left[30a^2\alpha_v(\Delta t)^3 - 6a^4(\Delta t)^4 + (\Delta x)^4\right]\frac{\partial^5 U}{\partial x^5}$$
$$+ O\left[(\Delta x)^5\right] \tag{43}$$

and

$$\frac{\partial U}{\partial t} + a\frac{\partial U}{\partial x} - \alpha_v \frac{\partial^2 U}{\partial x^2} = \frac{a}{360}\left[3a(\Delta t)^4 + 2(\Delta x)^4\right]\frac{\partial^5 U}{\partial x^5} + O\left[(\Delta x)^5\right] \tag{44}$$

As expected, no space-time coupling terms exist. In each of these schemes, the first occurrence of purely viscous error terms ($a = 0$) is associated with $\frac{\partial^6 U}{\partial x^6}$. To retain the formal accuracy of a scheme with errors $(\Delta t)^p$ and $(\Delta x)^q$, the modified equation must only contain terms proportional to $(\Delta t)^r$, $(\Delta x)^s$, and $(\Delta t)^R(\Delta x)^S$, where $r \geq p$, $s \geq q$, and $S + R \geq \min(p, q)$. The accuracy of the schemes is verified in the absence of boundaries for the convection-diffusion equation. A nonlinear viscous accuracy analysis of the schemes in the absence of boundaries is presented in appendix C and shows that viscous terms are calculated to the same accuracy as inviscid ones and that the schemes retain their advertised accuracy on the nonlinear problem.

Numerical Boundary Conditions

In each of the numerical schemes presented, a special procedure must be derived to evaluate the derivatives at the computational boundary points. Because accurate interior-scheme stencils are usually large, typically at least the derivatives at the boundary grid points require a noncentered stencil. To preserve the formal accuracy of a spatially Nth-order accurate interior scheme on hyperbolic equations, the boundary and near-boundary points must be closed with stencils that are no less than $(N-1)$th order. (See ref. 50.) The procedure to derive higher order implicit and explicit boundary stencils with a symbolic manipulator is straightforward. (See appendix A.) Unfortunately, schemes using these higher order (fourth-order and greater) stencils are most often unstable (refs. 16 and 51); hence, they are inappropriate to implement computationally. Although lower order approximations to the derivative at the boundary points degrade the formal accuracy of the entire numerical method, from a practical standpoint, this degradation is only observed if the boundaries are a primary source of error. Therefore, if a stable, high-order boundary condition is available for an interior scheme, it is used. If not, the more forgiving, lower order formulations are used. For the viscous derivatives, viscous derivative boundary conditions in this study are closed to the same order as the viscous interior operator; Nth-order inviscid central derivative operators are closed no greater than $(N-1)$th order. An unforeseen result of this study is that closing the boundary points of the dissipative interior stencils cannot be done by simply using boundary closures derived for the centered-difference Runge-Kutta schemes. Formally, all extended MacCormack and RKLW schemes are (2-2) schemes because of an interaction of the boundary and interior stencils of the inviscid

derivative operator. The problem is not relegated to only these two families of schemes; it affects the (2-4) scheme by Gottlieb and Turkel and is likely to affect other dissipative schemes. For simplicity, the truncation error is derived for one time step in the form of a modified equation for the seven boundary points used in the discretization of the equation $U_t + U_x = 0$ with the RKLW integrator and the explicit inviscid stencil of Gottlieb and Turkel (3-4E(GT)) RKLW as follows:

Grid point 1:

$$U_t + U_x = -\frac{\lambda\ (7+17\lambda)}{108}\Delta x - \frac{\sqrt{-1}\lambda\,(18+55\lambda)}{162}(\Delta x)^2 + O\left[(\Delta x)^3\right]$$

Grid point 2:

$$U_t + U_x = -\frac{\lambda\,(-5+7\,\lambda)}{108}\Delta x - \frac{\sqrt{-1}\lambda\,(-27+23\lambda)}{324}(\Delta x)^2 + O\left[(\Delta x)^3\right]$$

Grid point 3:

$$U_t + U_x = \frac{\lambda\,(84+55\lambda)}{1296}\Delta x + \frac{\sqrt{-1}\lambda\,(24+23\lambda)}{324}(\Delta x)^2 + O\left[(\Delta x)^3\right]$$

Grid point 4:

$$U_t + U_x = \frac{\lambda\,(-4+17\lambda)}{432}\Delta x + \frac{\sqrt{-1}\lambda\,(-12+55\lambda)}{1296}(\Delta x)^2 + O\left[(\Delta x)^3\right]$$

Grid point 5:

$$U_t + U_x = -\frac{5\lambda^2}{432}\Delta x - \frac{\sqrt{-1}\lambda^2}{81}(\Delta x)^2 + O\left[(\Delta x)^3\right]$$

Grid point 6:

$$U_t + U_x = \frac{\lambda^2}{1296}\Delta x + \frac{\sqrt{-1}\lambda^2}{1296}(\Delta x)^2 + O\left[(\Delta x)^3\right]$$

Grid point 7:

$$U_t + U_x = O\left[(\Delta x)^3\right]$$

The initial condition is $\exp[i(x)]$ with a boundary condition $\exp[i(-t)]$. The exact solution is $\exp[i(x-t)]$. No physical boundary conditions are imposed at intermediate levels of the scheme, a technique which has been shown elsewhere (ref. 52) to be higher order. Because of the lack of cancellation at the boundary, error terms of first order are generated at the first six grid points. The RKLW scheme is locally first-order accurate near the boundary and globally second-order accurate. Use of compact derivative operators would spread this error over the entire domain because of the fullness of the matrix **A** instead of confining it to only the boundaries.

Table 7 shows a grid refinement study of the (3-4E) Runge-Kutta scheme given in table 4 versus the (3-4E) RKLW scheme given in table 3. Note that in this one-dimensional problem the domain contains only 2 full wavelengths. Degradation from the boundaries requires significant resolution; full degradation of the RKLW scheme does not occur until resolutions on the order of 8000 grid points per wavelength. Machine precision becomes a factor as $\log_{10} L_2 < -9$.

Time-stable wall boundary stencils for the explicit fourth-order, centered first derivative operator are given by

$$f_1^{'} = \frac{1}{6\Delta x}(-11f_1 + 18f_2 - 9f_3 + 2f_4) \tag{45}$$

$$f_2^{'} = \frac{1}{6\Delta x}(-2f_1 - 3f_2 + 6f_3 - f_4) \tag{46}$$

$$f_1^{'} + 2f_2^{'} = \frac{1}{2\Delta x}(-5f_1 + 4f_2 + f_3) \tag{47}$$

for the compact, tridiagonal fourth-order operators. Each of these equations is third-order accurate and results in a formally fourth-order accurate inviscid derivative operator. A stable boundary stencil for the third-order viscous operator is given by

$$f_1^{'} = \frac{1}{6\Delta x}(-11f_1 + 18f_2 - 9f_3 + 2f_4) \tag{48}$$

To close the boundary point $f^{'}_{nx-(i-1)}$, the negative complex conjugate of the Fourier image of the stencil at $f_i^{'}$ is utilized; this means for the stencil

$$f_i' = \cdots + \frac{b_L f_{i-2}}{\Delta x} + \frac{a_L f_{i-1}}{\Delta x} + \frac{\Upsilon f_i}{\Delta x} + \frac{a_R f_{i+1}}{\Delta x} + \frac{b_R f_{i+2}}{\Delta x} + \cdots \tag{49}$$

that

$$f'_{nx-(i-1)} = \cdots - \frac{b_R f_{nx-(i+1)}}{\Delta x} - \frac{a_R f_{nx-(i)}}{\Delta x} - \frac{\Upsilon f_{nx-(i-1)}}{\Delta x} - \frac{a_L f_{nx-(i-2)}}{\Delta x} - \frac{b_L f_{nx-(i-3)}}{\Delta x} - \cdots \tag{50}$$

where nx is the number of grid points. Closure stencils for the viscous interior stencils must be closed with some care because a different number of points must be closed on the two sides of the computational domain. For the explicit stencils used in this study for the $(N-1)$th-order accurate viscous derivative operators, $(N-1)$ boundary points need to be closed. The forward operator requires $N/2$ points to be closed at the right computational boundary and $(N-2)/2$ points at the left computational boundary. This reverses when the backward viscous interior derivative operator is used. For example, the third-order viscous interior derivative operator is closed with expressions for $f_1^{'}$, $f_2^{'}$, $f_{nx}^{'}$ on the forward stage and $f_1^{'}$, $f_{nx}^{'}$, $f_{nx-1}^{'}$ on the backward stage. The most interior point of these, $f_2^{'}$ or $f_{nx-1}^{'}$, depending on which stage is being used, is closed with the negative complex conjugate of the interior stencil. Further discussion of boundary closures focuses on the computational domain containing the leftmost boundary points.

Stable, fifth-order accurate boundary stencils for the centered-difference stencils are given by

$$f_1^{'} = \frac{1}{60\Delta x}(-197f_1 + 690f_2 - 1380f_3 + 1850f_4 - 1575f_5 + 822f_6 - 240f_7 + 30f_8) \tag{51}$$

$$f_2^{'} = \frac{1}{60\Delta x}(-18f_1 - 35f_2 + 66f_3 - 30f_4 + 50f_5 - 57f_6 + 30f_7 - 6f_8) \tag{52}$$

$$f_3^{'} = \frac{1}{60\Delta x}(+3f_1 - 30f_2 - 20f_3 + 60f_4 - 15f_5 + 2f_6) \tag{53}$$

for the explicit sixth-order derivative operator, by

$$f_1^{'} = \frac{1}{1680\Delta x}(-4736f_1 + 14525f_2 - 26250f_3 + 34475f_4 - 30100f_5 + 16611f_6 - 5250f_7 + 725f_8) \tag{54}$$

$$f_2' = \frac{1}{720\Delta x}(-135f_1 - 844f_2 + 1635f_3 - 1050f_4 + 575f_5 - 240f_6 + 69f_7 - 10f_8) \tag{55}$$

for the compact tridiagonal sixth-order derivative, and by

$$f_1' = \frac{1}{1500\Delta x}(-4639f_1 + 14790f_2 - 25746f_3 + 29370f_4 - 20205f_5 + 7674f_6 - 1250f_7 + 6f_8) \tag{56}$$

$$f_2' = \frac{1}{4500\Delta x}(-1416f_1 - 1979f_2 + 2460f_3 + 2820f_4 - 2240f_5 - 129f_6 + 684f_7 - 200f_8) \tag{57}$$

for the compact pentadiagonal sixth-order derivative operator.

Results for the compact tridiagonal sixth-order derivative operator were first given by Carpenter (ref. 16). These results are referred to as $5^2, (5^2\text{-}6\text{-}5^2), 5^2$ schemes and are formally sixth-order accurate in space. By using $(\#fp)$ to designate the number of free parameters and O_i' to denote the order of accuracy of the first derivative approximation to a function f at grid point i, we designate schemes with as

$$\left(O_1'^{(\#fp)}, O_2'^{(\#fp)}, \cdots - O_{\text{interior}} - \cdots, O_{nx-1}'^{(\#fp)}, O_{nx}'^{(\#fp)}\right) \tag{58}$$

An $(N-1)$th-order explicit stencil representing an approximation to f' requires N grid points. By extending the stencil to $(N+2)$ grid points, two degrees of freedom are added through two free parameters. The expression 5^2 implies a fifth-order accurate stencil with two free parameters using an eight point stencil. To determine the minimum number of grid points needed to be closed for a centered-difference interior derivative operator, the bandwidths for matrices $\mathbf{P}$ and $\mathbf{Q}$ must be considered. If the matrix with the larger bandwidth has a bandwidth of ϕ, then $(\phi - 1)/2$ boundary grid points must be closed on each side of the computational domain. Where eighth-order spatial accuracy and higher is desired, additional boundary stencils are added to allow sufficient degrees of freedom for a stable boundary closure to be obtained. For eighth-order accuracy, four boundary grid points were needed at each end, each with four degrees of freedom. Closure of tenth-order schemes may be done with six boundary grid points, each with six degrees of freedom.

The boundaries are closed to lower order for the compact interior stencils by

$$f_1' + 2f_2' = \frac{1}{2\Delta x}(-5f_1 + 4f_2 + f_3) \tag{59}$$

$$\frac{1}{4}f_1' + f_2' + \frac{1}{4}f_3' = \frac{3}{4\Delta x}(f_3 - f_1) \tag{60}$$

The explicit sixth-order interior scheme uses the same three wall points as the fourth-order explicit scheme. Both schemes are formally fourth-order accurate and are referred to as the (3,4-6-4,3) and (3,3,4-6-4,3,3) schemes.

Fifth-order accurate boundary stencils for the fifth-order viscous operator, which are used in several extended MacCormack and RKLW schemes, are given by

$$f_1' = \frac{1}{60\Delta x}(-137f_1 + 300f_2 - 300f_3 + 200f_4 - 75f_5 + 12f_6) \tag{61}$$

$$f_2' = \frac{1}{60\Delta x}(-12f_1 - 65f_2 + 120f_3 - 60f_4 + 20f_5 - 3f_6) \tag{62}$$

Boundary conditions for higher order schemes are contained in appendix D. Note that stable high-order boundary stencils for one scheme are likely to be violently unstable if used with a different interior scheme.

All proposed central-difference stencils have been verified to have bounded left-half-plane eigenvalues for the matrix $\mathbf{A}$. This condition is necessary for stability of Runge-Kutta schemes but does not guarantee stability for Navier-Stokes calculations. Table 8 gives the value of the real part $\Re$ of the eigenvalue of the matrix $\mathbf{A}$, which has the largest real component for various grid sizes. In each case, the largest real component of any derivative operator is contained in the left half of the complex plane. This notation indicates that the derivative operators will be time-stable.

In addition, the stability of all predictor-corrector (RKLW and extended MacCormack) schemes has also been investigated for bounded left-half-plane eigenvalues of the matrix $\mathbf{M} = \frac{1}{2}\left(\mathbf{A}^{+}\mathbf{A}_v^{-} + \mathbf{A}^{-}\mathbf{A}_v^{+}\right)$. Several of the schemes listed have eigenvalues in the right-half-plane and are unstable; for instance, all (2-6P), (2-8T), (3-6P), and extended MacCormack and RKLW schemes using seventh-order boundary stencils are unstable. The value of the largest real eigenvalue of $\mathbf{M}$ is given in table 9. Again, these schemes are only formally (2-2) schemes in the presence of numerical boundaries.

Filters

In reasonably well-resolved computations, numerical errors are still present and are introduced primarily at high wave numbers. This can readily be seen by plotting the Fourier image of the finite-difference first derivative versus the spectral derivative or, as is sometimes stated, modified wave number versus wave number. (See ref. 13.) Figure 5 shows the accuracy of various centered-difference first derivatives relative to the exact spectral derivative. It is immediately apparent that compact derivative operators ($\mathbf{P} \neq \mathbf{I}$) are more accurate than their explicit counterparts because the representation of Ψ as a polynomial is most accurately done as a Padé approximate. All derivative operators have no resolution at $\xi = \pi$ and have marginal resolution for wave numbers near π. Nonlinear interaction of these unresolved, nonphysical waves of various wave numbers generates higher wave-number information. When the grid is unable to resolve the highest wave-number information, the error is introduced into low wave numbers and eventually contaminates the solution. In addition, successive application of the first derivative operator to obtain a second-order derivative results in an amplification factor of unity at $\xi = \pi$ for centered-difference operators; this application facilitates what is commonly referred to as "odd-even" decoupling. To suppress these effects, a numerical filter is used to create artificial viscosity. Several criteria exist for a useful filter. Eigenvalues that correspond to low wave numbers that are resolved should be virtually untouched; the relatively unresolved high wave numbers should be removed. Either an explicit or implicit filter can be chosen. Although Lele (ref. 13) uses implicit filters up to sixth order, in this study an explicit filter is used because it is computationally more efficient and its design is more conceptually straightforward. As a filtering function, we seek a function that is equal to 0 at $\xi = \pi$ and is equal to 1 at $\xi = 0$. A simple function to satisfy this need is

$$1 - \sin^{2n}\frac{\xi}{2} \tag{63}$$

We also desire a filter whose accuracy may be chosen arbitrarily; the filtering function must have a slope that approaches 0 to the chosen order as ξ approaches 0. Thus a $(2n)$th-order filter should have, to leading order, $\Psi = \xi^{2n}$ because ξ tends to zero. The magnitude of the filter must also be equal to or less than 1. Several discussions of filtering approaches can be found in the literature. (See refs. 19, 18, 17, and 53.) This discussion follows that of Eriksson (ref. 54), who derived explicit filters of second, fourth, and sixth order.

For the finite-difference implementation of these filters, begin with the following definition of the explicit central-difference operator for the $(2n)$th-order derivative of a function f:

$$f_i^{(2n)} = \frac{\Upsilon f_i}{(\Delta x)^{(2n)}} + a\frac{f_{i+1} + f_{i-1}}{(\Delta x)^{(2n)}} + b\frac{f_{i+2} + f_{i-2}}{(\Delta x)^{(2n)}} + c\frac{f_{i+3} + f_{i-3}}{(\Delta x)^{(2n)}} + d\frac{f_{i+4} + f_{i-4}}{(\Delta x)^{(2n)}} + \cdots \tag{64}$$

and the Fourier image given by

$$\Psi = \Upsilon + 2a\ \cos(\xi) + 2b\ \cos(2\xi) + 2c\ \cos(3\xi) + 2d\ \cos(4\xi) + \cdots \tag{65}$$

If consideration is given only to the second-order accurate versions of these derivatives, the negatives of the coefficients are given in table 10.

In Fourier space, the second-order accurate stencil of $\left[\frac{\partial^{2n} f}{\partial x^{2n}}\right]$, $\Psi = \xi^{2n} + O(\xi^{2n+2})$, is given by

$$\Psi = (-1)^{n+1} \left(2\ \sin\ \frac{\xi}{2}\right)^{2n} \tag{66}$$

Table 10 shows the terms proportional to the interior stencil coefficients for filters of orders 2 ($n = 1$) through 20 ($n = 10$).

If we choose a matrix filter function $\mathbf{D}$ that is symmetric, then it has real eigenvalues. Because this filter function is based on a stencil that, when implemented with the temporal schemes discussed, has eigenvalues that are negative, then $U_i D_{ij} U_j$ is always negative. This negative value guarantees that the filter is completely dissipative. The filter function is implemented on a vector $\mathbf{U}$ as $\widehat{\mathbf{U}} = (1 + \alpha_D \mathbf{D})\mathbf{U}$, where $\widehat{\mathbf{U}}$ is the filtered vector; α_D must be given by $(-1)^{n+1} 2^{-2n}$ for a $(2n)$th-order filter. Figure 6 shows the filter strength in Fourier space.

To close the matrix $\mathbf{D}$ at the boundaries and retain symmetry, skewed stencils of order n are used with an interior scheme of order $2n$. Appendix E contains the upper left portions of the matrix $\mathbf{D}$ for filters of orders two through twenty ($n = 1 - 10$). A formally tenth-order accurate scheme may now be closed with no concern as to how the boundary points of the filter affect the spatial operator.

Results

Because of the large number of schemes presented in the text, the number of permutations of boundary closures possible, and run times of several hours, only a few of the schemes could be run on large grids. The flow field of interest was the spatially evolving, two-dimensional, compressible nitrogen-hydrogen shear layer. This flow field was chosen because regions of intense gradients occur both near and far from the flow centerline; this makes grid allocation difficult and places a heavy burden on the accuracy and computational stability of the numerical method. It is also an important prelude to the supersonic, hydrogen-air, reacting shear layer found in scramjet combustors.

Inflow conditions to all computations are Euler supersonic (ref. 55) and are described elsewhere in reference 1. They represent a self-similar, supersonic, nitrogen-hydrogen shear layer with $\mathrm{Ma}_c = 0.45$, where Ma_c is the convective Mach number. The inflow shear-layer thickness was fixed at 2 mm. A factor of 100 between the shear-layer thickness and the transverse domain was used to ensure that no reflections from the inflow plane returned to the shearing region before the domain ended. Forcing was applied at the inflow to the transverse velocity component in the form of a sinusoidal disturbance. Amplitudes of 4 and 2 percent of the mean velocity were applied to the fundamental and subharmonic frequencies, respectively. No attempt was made to adjust other inflow variables to preserve consistency with the governing equations in the presence of this forcing. A result of this was a strong adjustment zone immediately downstream of the inflow plane where large amplitude disturbances propagated toward the transverse boundaries, potentially contaminating the shearing region with spurious boundary reflection. The forcing profile of the transverse velocity was in the form of a near step function centered at the region of maximum velocity gradient and falling off precipitously at the shear-layer edge; this was found to minimize the amplitude of the disturbances impinging on the transverse boundaries.

Principal runs were done on grids of 301 by 451 with transverse grid clustering to represent a physical domain of 200 by 100 mm. Only about 10 percent of the grid points was contained in the high-shearing

regions of the shear layer because of this choice. The four schemes investigated were the (2-4T), (2-6T), (3-4T) RKLW, and (3-6T) RKLW. No Runge-Kutta schemes are listed because several attempts were made to use the (4-4T) and (4-6T) schemes but they lacked sufficient dissipation to remain stable on the grid densities that were run. Boundary closures for the fourth- and sixth-order schemes were implemented as (3-4-3) and (3,4-6-4,3). These combinations were chosen because they were believed to represent the most practical schemes for these shear-layer simulations. All computations used Euler nonreflecting boundary conditions (refs. 56 and 57) at the two transverse boundaries and supersonic Euler boundary conditions at the outflow.

Differences in accuracy between the filtered (2-4T), (2-6T), (3-4T) RKLW, and (3-6T) RKLW schemes were not striking. Flow-field variables like velocity, pressure, temperature, and, more importantly, the differentiated quantities, vorticity and dilatation, were nearly independent of the scheme. All attempted schemes used a tridiagonal derivative operator that was chosen to reduce the truncation error of the derivative operator but caused a small increase in computational time due to the inversion of the matrix $\mathbf{P}$. Table 11 lists the truncation errors for various first-order derivatives, including several stencils not considered in any schemes in this paper. The explicit stencils have large truncation errors relative to the compact stencils; this is consistent with figure 5. Truncation error is minimum for the 4T, 6T, 8P, and 10P stencils. Further discussion of this situation is contained in appendix A. The penalty associated with the large CFL limits of the explicit versions of the various schemes in figures 1 through 4 is now clear—explicit stencils have large truncation errors. Inspection of terms that require significant resolution, such as $\nabla \times \omega$ and the dilatation gradient, in well-resolved simulations could help determine the efficacy of sixth-, eighth-, and tenth-order accurate schemes. Schemes with spatial accuracy greater than 10 may be readily derived by extending the current methodology; however, spectral schemes should probably be considered as an alternative for such highly resolved computations.

Computational stability was found to be more sensitive to numerical method than accuracy. Extended MacCormack schemes are more stable than the RKLW schemes and far more stable than the Runge-Kutta schemes. Several runs on smaller grid densities with the (4-4T) and (4-6T) schemes were completed for nitrogen-nitrogen shear layers; this suggests that the robustness required for disparate-mass gas mixtures is significantly greater. Modifying the temporally third-order Runge-Kutta scheme with the addition of the predictor-corrector sequence to form the RKLW family of schemes noticeably increases computational stability. Higher order numerical boundary conditions are presented; however, they are not used because dissipative schemes are, by definition, lower order at the boundary. In smaller nitrogen-nitrogen simulations with the (4-4T) and (4-6T) schemes, the formally accurate boundary closures were found to be less forgiving than the lower order closures and were more likely to lead to computational instability on any given grid. This conclusion is based on the closure response to the manner in which the shear layer was forced. Inadequate resolution and minimal dissipation from both the interior and boundary stencils make the Runge-Kutta schemes impractical for these simulations until grid densities become significantly greater than those chosen here.

The appropriate choice of schemes depends strongly on the accuracy, computational stability, and CFL limits of the method and the needs and resources of the user. For smaller grid densities where robustness was more important than CPU time, the (2-4T) scheme was very useful. The (2-6T) scheme was slightly slower. On larger grid sizes, such as 301 by 451, the (3-6T) RKLW scheme was preferred because it was slightly more accurate and actually faster than the (2-4T). A comparison of run times indicates that the RKLW schemes may be run to the same physical time as its corresponding extended MacCormack scheme (i.e., (3-4T) RKLW versus (2-4T)), in significantly less CPU time. Relative to the (2-4T) scheme, the run times of the (2-6T), (3-4T) RKLW, and (3-6T) RKLW schemes are 1.24, 0.75, and 0.92, respectively. The (3-8T) RKLW scheme is likely to require only 11 percent more CPU time than the (2-4T) scheme. Although we did not attempt to run any of the explicit dissipative schemes, they have significantly larger stability envelopes, are easy to code, require no inversion of the matrix $\mathbf{P}$, and are, consequently, likely to be very fast. Pentadiagonal schemes were presented here up to tenth order; however, these schemes may

not be considered competitive because of the difficulty in inverting **P** until the truncation-error penalty of the explicit or tridiagonal stencils is deemed sufficiently large.

A surprising finding in this work is the effect of filters. Filtering was applied to the vector **U** after all full predictor-corrector and central-difference stages in order to remove spurious information before it could move to lower wave numbers. The unfiltered dilatation field for the dissipative (2-4T) scheme was badly contaminated; filtering resulted in a noticeable improvement. Figures 7(a) and 7(b) show a section of the dilatation field from a 101 by 151 simulation using the (2-4T) scheme of a nitrogen-nitrogen shear layer at $\mathrm{Ma}_c = 0.45$, with and without filtering. For comparison purposes, a very large 401 by 601 simulation was run with the (3-6T) RKLW scheme. (See fig. 7(c).) The filters were found to improve the calculations more than any differences in temporal or spatial order of accuracy between the schemes. All runs were made with the tenth-order filter to avoid lowering the order of the $5^2, 5^2$-6-5^2,5^2 schemes. The appropriate filter order was chosen based on either the interior or boundary accuracy of the differencing scheme. The strongest filter that did not degrade the accuracy of either the interior or boundary points was used (i.e., the interior filter order could be no less than the order of the interior scheme nor could the filter boundary order be less than the boundary order of the scheme). A twentieth-order filter could then be used with a formally tenth-order scheme.

The fact that the filters had such a significant effect indicates that the simulations may not have been completely resolved. To determine whether a calculation is well resolved, a good test (in addition to grid refinement) is to compare filtered and unfiltered simulations. Dilatation was a particularly sensitive variable to resolution. The 301 by 451 calculations should be considered "model-free simulations" but not "direct numerical simulations." Later simulations of the nitrogen-hydrogen shear layer at $\mathrm{Ma}_c = 0.45$ on the 401 by 601 grid were believed to be fully resolved because contours of third derivatives of the velocity were not only smooth but also physically plausible. Model-free simulations that "run" are no guarantee that all relevant scales of the problem are resolved.

In addition, misspecification of the physical boundary conditions, which is a current topic of research, becomes more apparent as the accuracy of the method is increased. For sufficiently refined grids, supersonic Euler outflow boundary conditions are clearly inadequate in the center of the shear layer. Dilatation provides a simple tool to gauge whether the nonreflecting physical boundary conditions used on the upper and lower boundaries were, in fact, reflecting. Vorticity contours give virtually no indication of this boundary contamination.

Concluding Remarks

An investigation was conducted of several numerical schemes that offered high spatial and temporal accuracy and were used in the computation of two-dimensional, spatially evolving, laminar, variable-density compressible shear layers. Three schemes with various temporal accuracies and arbitrary spatial accuracy of both the inviscid and viscous terms were presented and analyzed. All integration schemes made use of explicit or compact finite-difference derivative operators. Extended MacCormack schemes retained the robustness of the original, uniformly second-order accurate method. Spatial accuracy was enhanced, and the stability limit was somewhat restricted. Extending the original MacCormack scheme resulted in longer run times; however, simulations achieved far greater spatial resolution. The (2-4T) scheme, used in conjunction with a tenth-order filter, provided an accurate, computationally stable, general purpose numerical scheme. For large, well-resolved simulations where computational stability (dissipation) was not as critical, the temporally third-order RKLW (Rusanov-Kutler-Lomax-Warming) scheme was preferred. As with the extended MacCormack schemes, spatial accuracy of both the inviscid and viscous terms could be chosen freely. Stability limits of the RKLW scheme were large because of strong resemblance to the Runge-Kutta central-difference schemes. Computational stability was achieved by the same space-time dissipative terms in the extended MacCormack schemes. This approach made the RKWL schemes more stable than the Runge-Kutta schemes with the same workload per stage. An additional benefit of the extended MacCormack and RKLW schemes was that computer codes written

with the original MacCormack or Gottlieb-Turkel scheme may be readily upgraded to higher temporal and spatial accuracy with minimal effort. Third- and fourth-order Runge-Kutta schemes, although very accurate, possessed insufficient dissipation for the calculations conducted in this work. Filters did not add enough dissipation to stabilize computations with significant compressibility and variable-density effects. Tridiagonal difference operators were chosen for their low truncation error. Pentadiagonal operators are not likely to be competitive below eighth-order accuracy.

In each of the schemes, stability was considered for the interior operators in the convection-diffusion equation $U_t + aU_x = \alpha_v U_{xx}$. Accuracy of the extended MacCormack and RKLW schemes was verified for the nonlinear problem $U_t + F_x = 0$ and the viscous problem $U_t = [b(x)U_x]_x$. Numerical boundary treatments for Runge-Kutta schemes of various orders of accuracy were chosen and evaluated to be asymptotically stable. Derived, formally accurate boundary conditions were given for explicit sixth-order, pentadiagonal sixth-order, and explicit, tridiagonal, and pentadiagonal eighth-order central-difference operators. Lower order closures were also presented and shown to be stable. All boundary closures for the extended MacCormack and RKLW schemes were determined to destroy the formal accuracy of the schemes; this problem is a serious limitation of these schemes and is likely to occur in many other common dissipative schemes. Apparently, this problem has gone unnoticed for over two decades.

Damping of high wave-number, nonphysical data was accomplished for all schemes with the use of explicit filters. Filters have been derived up to tenth order on the boundaries and twentieth order in the interior. These filters use explicit finite-difference stencils, are computationally efficient, and act predominately on high wave-number data. Results of several simulations indicate that on moderately well-resolved simulations, the effects of temporal and spatial accuracy differences between the schemes were less important than filtering effects.

NASA Langley Research Center
Hampton, VA 23681-2199
July 31, 1997

Appendix A

Derivation of General Stencils

To generate the centered finite-difference approximation of $\frac{\partial^k f}{\partial x^k}$ to Nth-order accuracy, the problem is divided into cases with k even and odd. When $k = 2n-1$ is odd, the stencil is

$$\begin{aligned}
&\cdots + \delta[f_{i-4}^{(2n-1)} + f_{i+4}^{(2n-1)}] + \gamma[f_{i-3}^{(2n-1)} + f_{i+3}^{(2n-1)}] + \beta[f_{i-2}^{(2n-1)} + f_{i+2}^{(2n-1)}] \\
&\quad + \alpha[f_{i-1}^{(2n-1)} + f_{i+1}^{(2n-1)}] + f_i^{(2n-1)} \\
&= a\frac{f_{i+1} - f_{i-1}}{(\Delta x)^{(2n-1)}} + b\frac{f_{i+2} - f_{i-2}}{(\Delta x)^{(2n-1)}} + c\frac{f_{i+3} - f_{i-3}}{(\Delta x)^{(2n-1)}} \\
&\quad + d\frac{f_{i+4} - f_{i-4}}{(\Delta x)^{(2n-1)}} + e\frac{f_{i+5} - f_{i-5}}{(\Delta x)^{(2n-1)}} + f\frac{f_{i+6} - f_{i-6}}{(\Delta x)^{(2n-1)}} + \cdots
\end{aligned} \tag{A1}$$

and its Fourier image is written as

$$\Psi = \frac{i[2a\ \sin(\xi) + 2b\ \sin(2\xi) + 2c\ \sin(3\xi) + 2d\ \sin(4\xi) + 2e\ \sin(5\xi) + \cdots]}{[1 + 2\alpha\ \cos(\xi) + 2\beta\ \cos(2\xi) + 2\gamma\ \cos(3\xi) + 2\delta\ \cos(4\xi) + \cdots]} \tag{A2}$$

Expanding the sine and cosine functions as a Taylor series gives

$$\Psi = i\sum_{m=1}^{\infty} \psi_{(2m-1)}\xi^{(2m-1)} \tag{A3}$$

where the functions of $\psi_{(2m-1)}$ are $(a, b, \cdots, \alpha, \beta, \cdots)$. It is required that $\Psi = (i\xi)^k + O(\xi^{N+k})$ to approximate the spectral derivative to order N. A tenth-order pentadiagonal approximation to f''' may be obtained by solving six $\left(\frac{N+k-1}{2}\right)$ simultaneous equations ($\psi_1 = \psi_5 = \psi_7 = \psi_9 = \psi_{11} = 0$ and $\psi_3 = -1$) in six unknowns ($\alpha, \beta, a, b, c,$ and d). Solutions do not always exist for these stencils. Similarly, when $k = 2n$ is even, then the stencil is

$$\begin{aligned}
&\cdots + \delta[f_{i-4}^{(2n)} + f_{i+4}^{(2n)}] + \gamma[f_{i-3}^{(2n)} + f_{i+3}^{(2n)}] + \beta[f_{i-2}^{(2n)} + f_{i+2}^{(2n)}] + \alpha[f_{i-1}^{(2n)} + f_{i+1}^{(2n)}] + f_i^{(2n)} \\
&= \Upsilon\frac{f_i}{(\Delta x)^{(2n)}} + a\frac{f_{i+1} + f_{i-1}}{(\Delta x)^{(2n)}} + b\frac{f_{i+2} + f_{i-2}}{(\Delta x)^{(2n)}} + c\frac{f_{i+3} + f_{i-3}}{(\Delta x)^{(2n)}} \\
&\quad + d\frac{f_{i+4} + f_{i-4}}{(\Delta x)^{(2n)}} + e\frac{f_{i+5} + f_{i-5}}{(\Delta x)^{(2n)}} + f\frac{f_{i+6} + f_{i-6}}{(\Delta x)^{(2n)}} + \cdots
\end{aligned} \tag{A4}$$

and its corresponding Fourier image is given by

$$\Psi = \frac{[\Upsilon + 2a\ \cos(\xi) + 2b\ \cos(2\xi) + 2c\ \cos(3\xi) + 2d\ \cos(4\xi) + 2e\ \cos(5\xi) + \cdots]}{[1 + 2\alpha\ \cos(\xi) + 2\beta\ \cos(2\xi) + 2\gamma\ \cos(3\xi) + 2\delta\ \cos(4\xi) + \cdots]} \tag{A5}$$

or

$$\Psi = \sum_{m=1}^{\infty} \psi_{(2m-2)}\xi^{(2m-2)} \tag{A6}$$

A tenth-order heptadiagonal approximation to f^{VI} may be obtained by solving eight $\left(\frac{N+k}{2}\right)$ simultaneous equations ($\psi_0 = \psi_2 = \psi_4 = \psi_8 = \psi_{10} = \psi_{12} = \psi_{14} = 0$ and $\psi_6 = -1$) in eight unknowns ($\alpha, \beta, \gamma, a, b, c, d,$ and e). Again, it is required that $\Psi = (i\xi)^k + O(\xi^{N+k})$.

For arbitrary skewed stencils representing the kth derivative, we may write

$$\begin{aligned}
&\cdots + \delta_L f_{i-4}^{(k)} + \delta_R f_{i+4}^{(k)} + \gamma_L f_{i-3}^{(k)} + \gamma_R f_{i+3}^{(k)} + \beta_L f_{i-2}^{(k)} + \beta_R f_{i+2}^{(k)} \\
&\quad + \alpha_L f_{i-1}^{(k)} + \alpha_R f_{i+1}^{(k)} + f_i^{(k)} \\
&= \Upsilon \frac{f_i}{(\Delta x)^{(k)}} + \frac{a_L f_{i-1} + a_R f_{i+1}}{(\Delta x)^{(k)}} + \frac{b_L f_{i-2} + b_R f_{i+2}}{(\Delta x)^{(k)}} + \frac{c_L f_{i-3} + c_R f_{i+3}}{(\Delta x)^{(k)}} \\
&\quad + \frac{d_L f_{i-4} + d_R f_{i+4}}{(\Delta x)^{(k)}} + \frac{e_L f_{i-5} + e_R f_{i+5}}{(\Delta x)^{(k)}} + \frac{f_L f_{i-6} + f_R f_{i+6}}{(\Delta x)^{(k)}} + \cdots
\end{aligned} \tag{A7}$$

and give its Fourier image by

$$\Psi = \frac{\left\{ \begin{array}{l} [\Upsilon + (a_R + a_L)\cos(\xi) + (b_R + b_L)\cos(2\xi) + (c_R + c_L)\cos(3\xi) + \cdots] \\ \quad + i[(a_R - a_L)\sin(\xi) + (b_R - b_L)\sin(2\xi) + (c_R - c_L)\sin(3\xi) + \cdots] \end{array} \right\}}{\left\{ \begin{array}{l} [1 + (\alpha_R + \alpha_L)\cos(\xi) + (\beta_R + \beta_L)\cos(2\xi) + \cdots] \\ \quad + i[(\alpha_R - \alpha_L)\sin(\xi) + (\beta_R - \beta_L)\sin(2\xi) + \cdots] \end{array} \right\}} \tag{A8}$$

or

$$\Psi = \sum_{m=1}^{\infty} \psi_{(2m-2)} \xi^{(2m-2)} + i \sum_{m=1}^{\infty} \psi_{(2m-1)} \xi^{(2m-1)} \tag{A9}$$

For the kth derivative, Ψ must be either purely imaginary (k is odd) or purely real (k is even). We now must solve $(N+k)$ simultaneous equations in $(N+k)$ unknowns: $\psi_k = (i)^k$ (for k even), $\psi_k = (i)^{k-1}$ (for k odd), and $\psi_l = 0, l = 0, 1, \cdots, (N+k-1), l \neq k$.

In the special case of the centered first derivative, let p denote the number of bands in the matrix $\mathbf{P}$, let q denote the number of bands in the matrix $\mathbf{Q}$, and let n be $N/2$. The order of the derivative N is then equal to $p+q-2$. Simple recursion relations for the coefficients of the matrix $\mathbf{P}$ can be found for $p \leq q$. Stencils for which $p > q$ are of marginal practical utility because they are computationally inefficient and have a larger truncation error than those with $p = q$. The following relations can be derived:

$$\alpha = \frac{(p-1)}{(p+1)} \frac{[N-(p-1)]}{[N-(p-3)]} \tag{A10}$$

$$\beta = \frac{(p-3)(p-1)}{(p+3)(p+1)} \frac{[N-(p+1)][N-(p-1)]}{[N-(p-5)][N-(p-3)]} \tag{A11}$$

$$\gamma = \frac{(p-5)(p-3)(p-1)}{(p+5)(p+3)(p+1)} \frac{[N-(p+3)][N-(p+1)][N-(p-1)]}{[N-(p-7)][N-(p-5)][N-(p-3)]} \tag{A12}$$

$$\delta = \frac{(p-7)(p-5)(p-3)(p-1)}{(p+7)(p+5)(p+3)(p+1)} \frac{[N-(p+5)][N-(p+3)][N-(p+1)][N-(p-1)]}{[N-(p-9)][N-(p-7)][N-(p-5)][N-(p-3)]} \tag{A13}$$

and so on.

For example, the thirty-second-order ($N = 32$) nonadiagonal ($p = 9$) first derivative has the coefficients $\alpha = 48/65$, $\beta = 132/455$, $\gamma = 176/3185$, and $\delta = 99/25480$.

Similar patterns can also be found in the matrix $\mathbf{Q}$ if $p \leq q$. For example,

$$a = \frac{4}{(p+1)^2} \frac{[pN - (p-1)^2](N+2)}{[N-(p-3)]^2} \tag{A14}$$

If we define

$$\left.\begin{aligned} \Phi &= \prod_{i=1}^{r} \left(\frac{i}{4i+2} \right) \\ \Gamma_z &= \prod_{i=1}^{z-r} \left(\frac{-i}{p+i} \right) \\ r &= \frac{p-1}{2} \end{aligned}\right\} \tag{A15}$$

then for $p = 1$ and 3,

$$b = \Phi \Gamma_1 \frac{[N-(p+1)][N-(p-1)]}{[N-(p-5)][N-(p-3)]} \tag{A16}$$

for $p = 1, 3$, and 5,

$$c = \Phi \Gamma_2 \frac{[N-(p+3)][N-(p+1)][N-(p-1)]}{[N-(p-7)][N-(p-5)][N-(p-3)]} \tag{A17}$$

for $p = 1, 3, 5$, and 7,

$$d = \Phi \Gamma_3 \frac{[N-(p+5)][N-(p+3)][N-(p+1)][N-(p-1)]}{[N-(p-9)][N-(p-7)][N-(p-5)][N-(p-3)]} \tag{A18}$$

and so on.

If we consider only explicit ($p = 1, \alpha = \beta = \cdots = 0$) central-difference stencils, then

$$a = +\frac{n-0}{n+1} \tag{A19}$$

$$b = -\frac{(n-0)(n-1)}{2(n+1)(n+2)} \tag{A20}$$

$$c = +\frac{(n-0)(n-1)(n-2)}{3(n+1)(n+2)(n+3)} \tag{A21}$$

$$d = -\frac{(n-0)(n-1)(n-2)(n-3)}{4(n+1)(n+2)(n+3)(n+4)} \tag{A22}$$

for the first derivative operators (first noted by Fornberg (ref. 58)), and

$$\Upsilon = -2(a+b+c+d+\cdots) \tag{A23}$$

$$a = +\frac{2}{(n+0)(n+1)} \tag{A24}$$

$$b = -\frac{2(n-1)}{(n+0)(n+1)(n+2)} \tag{A25}$$

$$c = +\frac{2(n-1)(n-2)}{(n+0)(n+1)(n+2)(n+3)} \tag{A26}$$

$$d = -\frac{2(n-1)(n-2)(n-3)}{(n+0)(n+1)(n+2)(n+3)(n+4)} \tag{A27}$$

for the second derivative operators.

Truncation error of centered first derivative operators can also be put in general formulas. The first derivative stencil truncation error for $p \leq q$ may be written as

$$-\frac{n!\,(n-r)!\,(r)!\,\prod_{i=1}^{r}(2i-1)}{(N+1)!\,\prod_{i=1}^{r}[2(n-i)+1]}\,\xi^{(N+1)} \tag{A28}$$

If we compare two different first derivative approximations that are each Nth-order accurate with the subscripts a and b distinguishing the two and let $r_a > r_b$, then the ratio of the truncation errors for $p \leq q$ is given by

$$\frac{(n-r_a)!\,(r_a)!\,\prod_{i=r_b+1}^{r_a}(2i-1)}{(n-r_b)!\,(r_b)!\,\prod_{i=r_b+1}^{r_a}[2(n-i)+1]} \tag{A29}$$

As r_a becomes progressively larger than r_b, the ratio becomes very small; this implies, for example, that for a twentieth-order derivative, a nonadiagonal derivative has far less truncation error than a tridiagonal derivative. Truncation error is minimized by letting $p = q$ ($N = 4, 8, 12, \cdots$) or $p = q - 2$ ($N = 2, 6, 10, \cdots$) for $p \leq q$. This approach has been empirically verified in cases where $p \leq 9$ for all possible values of q.

Appendix B

Low-Storage Runge-Kutta Methods

Consider the equation $U_t + F_x = 0$, where $F = F(U)$ and $F_x = F_U U_x = f U_x$. The traditional three-stage Runge-Kutta method may be represented in the equation $U_t = -F_x$ as

$$\left.\begin{aligned} U^* &= U^n - a_{21}\lambda f^n \mathbf{A} U^n \\ U^{**} &= U^n - a_{31}\lambda f^n \mathbf{A} U^n - a_{32}\lambda f^* \mathbf{A} U^* \\ U^{n+1} &= U^n - b_1\lambda f^n \mathbf{A} U^n - b_2\lambda f^* \mathbf{A} U^* - b_3\lambda f^{**} \mathbf{A} U^{**} \end{aligned}\right\} \tag{B1}$$

where $\mathbf{A}$ is the matrix derivative operator and $\lambda = \frac{\Delta x}{\Delta t}$. Alternatively, in Butcher array form (ref. 42), this appears as

$$\begin{array}{c|ccc} 0 & & & \\ c_2 & a_{21} & & \\ c_3 & a_{31} & a_{32} & \\ \hline & b_1 & b_2 & b_3 \end{array} \tag{B2}$$

In some cases, storage requirements of computations should be minimized. We briefly elaborate on the Runge-Kutta scheme given by Williamson (ref. 43). He derives formulas that allow storage of only two values (2M) of the vector $\mathbf{U}$, where $\mathbf{U}$ has a vector length M. In the low-storage format, this becomes

$$\left.\begin{aligned} q^n &= \lambda f^n \mathbf{A} U^n - A_1 q^{-*} \\ U^* &= U^n - B_1 q^n \\ q^* &= \lambda f^* \mathbf{A} U^* - A_2 q^n \\ U^{**} &= U^* - B_2 q^* \\ q^{**} &= \lambda f^{**} \mathbf{A} U^{**} - A_3 q^* \\ U^{n+1} &= U^{**} - B_3 q^{**} \end{aligned}\right\} \tag{B3}$$

or

$$\left.\begin{aligned} U^* &= U^n - B_1\lambda f^n \mathbf{A} U^n \\ U^{**} &= U^* - B_2(\lambda f^* \mathbf{A} U^* - A_2\lambda f^n \mathbf{A} U^n) \\ U^{n+1} &= U^{**} - B_3[\lambda f^{**} \mathbf{A} U^{**} - A_3(\lambda f^* \mathbf{A} U^* - A_2\lambda f^n \mathbf{A} U^n)] \end{aligned}\right\} \tag{B4}$$

Setting A_1 to zero creates a self-starting procedure. This procedure results in a one-parameter family of schemes. The relationship between low-storage and traditional methods may also be shown with the aid of

$$\begin{array}{c|ccc} 0 & & & \\ c_2 & a_{21} & & \\ c_3 & a_{31} & a_{32} & \\ \hline & b_1 & b_2 & b_3 \end{array} \quad \leftrightarrow \quad \begin{array}{c|ccc} 0 & & & \\ B_1 & B_1 & & \\ B_1 + B_2(A_2+1) & [A_2B_2 + B_1] & B_2 & \\ \hline & [A_2(A_3B_3 + B_2) + B_1] & (A_3B_3 + B_2) & B_3 \end{array} \tag{B5}$$

where $(A_1, A_2, B_1, B_2, B_3)$ correspond to the variables $(a_1, a_2, b_1, b_2, b_3)$ in Williamson's work. (See ref. 43.) Because the stability bounds of the two-parameter family of the third-order, three-stage Runge-Kutta method are independent of the parameter choice, the analysis presented in the text is valid for the low-storage formulas as well.

For $c_2 \neq 0, 2/3$, or c_3 and $c_3 \neq 0$, we define

$$\left.\begin{aligned}
z_1 &= \sqrt{(36c_2^4 + 36c_2^3 - 135c_2^2 + 84c_2 - 12)} \\
z_2 &= 2c_2^2 + c_2 - 2 \\
z_3 &= 12c_2^4 - 18c_2^3 + 18c_2^2 - 11c_2 + 2 \\
z_4 &= 36c_2^4 - 36c_2^3 + 13c_2^2 - 8c_2 + 4 \\
z_5 &= 69c_2^3 - 62c_2^2 + 28c_2 - 8 \\
z_6 &= 34c_2^4 - 46c_2^3 + 34c_2^2 - 13c_2 + 2
\end{aligned}\right\} \tag{B6}$$

The one-parameter family is given by

$$\left.\begin{aligned}
B_1 &= c_2 \\
B_2 &= \frac{12c_2(c_2-1)(3z_2-z_1) - (3z_2-z_1)^2}{144c_2(3c_2-2)(c_2-1)^2} \\
B_3 &= \frac{-24(3c_2-2)(c_2-1)^2}{(3z_2-z_1)^2 - 12c_2(c_2-1)(3z_2-z_1)} \\
A_2 &= \frac{-(6c_2^2-4c_2+1)z_1 + 3z_3}{(2c_2+1)z_1 - 3(c_2+2)(2c_2-1)^2} \\
A_3 &= \frac{-z_4 z_1 + 108(2c_2-1)c_2^5 - 3(2c_2-1)z_5}{24z_1c_2(c_2-1)^4 + 72c_2z_6 + 72c_2^6(2c_2-13)}
\end{aligned}\right\} \tag{B7}$$

which can be verified, provided that none of the respective denominators vanish. Williamson's optimized scheme appears in Butcher form as

$$\begin{array}{c|ccc}
0 & & & \\
\frac{1}{3} & \frac{1}{3} & & \\
\frac{3}{4} & -\frac{3}{16} & \frac{15}{16} & \\
\hline
 & \frac{1}{6} & \frac{3}{10} & \frac{8}{15}
\end{array}
\quad \rightarrow \quad
\begin{array}{c|c}
A_1 & B_1 \\
A_2 & B_2 \\
A_3 & B_3
\end{array}
\quad = \quad
\begin{array}{c|c}
0 & \frac{1}{3} \\
-\frac{5}{9} & \frac{15}{16} \\
-\frac{153}{128} & \frac{8}{15}
\end{array} \tag{B8}$$

Allen Wray of the Ames Research Center (personal communication) has considered cases where $c_2 = 2/3$.

If an extra stage is added, a three free-parameter family of low-storage schemes may be devised. Several schemes are given that are third-order accurate for the nonlinear problem and fourth-order accurate for the linear problem (F_U = Constant), where the stability bounds of the convection-diffusion equation are the largest for four-stage schemes. If we set $c_2 = c_3$, then

$$\begin{array}{c|cccc} 0 & & & & \\ \frac{1}{3} & \frac{1}{3} & & & \\ \frac{1}{3} & -\frac{5}{12} & \frac{3}{4} & & \\ 1 & \frac{1}{4} & \frac{1}{12} & \frac{2}{3} & \\ \hline & 0 & \frac{1}{3} & \frac{5}{12} & \frac{1}{4} \end{array} = \begin{array}{c|c} 0 & \frac{1}{3} \\ -1 & \frac{3}{4} \\ -1 & \frac{2}{3} \\ -1 & \frac{1}{4} \end{array} \tag{B9}$$

If we set $c_3 = c_4$, then

$$\begin{array}{c|cccc} 0 & & & & \\ \frac{1}{4} & \frac{1}{4} & & & \\ \frac{11}{12} & -\frac{11}{36} & \frac{11}{9} & & \\ \frac{11}{12} & \frac{419}{396} & -\frac{16}{9} & \frac{18}{11} & \\ \hline & -\frac{1}{11} & \frac{3}{4} & \frac{17}{66} & \frac{1}{12} \end{array} = \begin{array}{c|c} 0 & \frac{1}{4} \\ -\frac{5}{11} & \frac{11}{9} \\ -\frac{11}{6} & \frac{18}{11} \\ -\frac{182}{11} & \frac{1}{12} \end{array} \tag{B10}$$

and

$$\begin{array}{c|cccc} 0 & & & & \\ \frac{19}{36} & \frac{19}{36} & & & \\ \frac{3}{4} & -\frac{51}{76} & \frac{27}{19} & & \\ \frac{3}{4} & \frac{19}{36} & 0 & \frac{2}{9} & \\ \hline & \frac{13}{57} & \frac{27}{76} & \frac{1}{6} & \frac{1}{4} \end{array} = \begin{array}{c|c} 0 & \frac{19}{36} \\ -\frac{205}{243} & \frac{27}{19} \\ -\frac{243}{38} & \frac{2}{9} \\ -\frac{2}{9} & \frac{1}{4} \end{array} \tag{B11}$$

Appendix C

Nonlinear Analysis

Consider the equation $U_t + F_x = [b(x)U_x]_x$ in a periodic domain, where $b(x)$ is taken to be exact. Let $\mathbf{B} = b\mathbf{I}$ and $F_x = F_U U_x = fU_x$. The accuracy of the extended MacCormack (2-[$2n$]) and RKLW (3-[$2n$]) families of schemes is now verified (the first number representing the temporal accuracy and the [$2n$] representing the spatial accuracy of the overall schemes, viscous and inviscid) with viscous stencils whose order of accuracy is [$2n$-1]. This verification is done in two parts. First, the equation $U_t = [b(x)U_x]_x$ is examined to determine the accuracy of the viscous terms; second, for the equation $U_t + F_x = 0$ the nonlinear accuracy is verified. The analysis provided is somewhat different than that given in the section "Formal Accuracy." Previous researchers have investigated some of these issues for spatially fourth-order accurate MacCormack schemes (ref. 9). Use of the variable n as a superscript on the vector U represents the nth time step; otherwise, it denotes spatial accuracy of the derivative operator. In matrix notation, the RKLW scheme may be represented for the equation $U_t = [b(x)\, U_x]_x$ in matrix form as

$$\left.\begin{aligned} U^* &= [\mathbf{I} + \beta_1 \lambda_v^{'} \mathbf{A}^- \mathbf{B} \mathbf{A}_v^+] U^n \\ U^{**} &= [\mathbf{I} + \beta_1 \lambda_v^{'} \mathbf{A}^+ \mathbf{B} \mathbf{A}_v^-] U^* \\ U^{\#} &= [U^n + \beta_2 (U^{**} - U^n)] \\ U^{n+1} &= \frac{1}{3}[U^n + 2(\mathbf{I} + \lambda_v^{'} \mathbf{A}^{2n} \mathbf{B} \mathbf{A}^{2n}) U^{\#}] \end{aligned}\right\} \tag{C1}$$

where $\lambda_v^{'} = \frac{\Delta t}{(\Delta x)^2}$. If we let

$$\left.\begin{aligned} \mathbf{A}^+ &= \mathbf{A}^{2n} + \mathbf{X} \\ \mathbf{A}^- &= \mathbf{A}^{2n} - \mathbf{X} \\ \mathbf{A}_v^+ &= \mathbf{A}^{2n} + \mathbf{X}_v \\ \mathbf{A}_v^- &= \mathbf{A}^{2n} - \mathbf{X}_v \end{aligned}\right\} \tag{C2}$$

then we may define

$$\left.\begin{aligned} \mathbf{A}^{2n} \mathbf{B} \mathbf{A}^{2n} &= \mathbf{Z}_1 \\ \mathbf{A}^{2n} \mathbf{B} \mathbf{X}_v &= \mathbf{Z}_2 \\ \mathbf{X} \mathbf{B} \mathbf{A}^{2n} &= \mathbf{Z}_3 \\ \mathbf{X} \mathbf{B} \mathbf{X}_v &= \mathbf{Z}_4 \end{aligned}\right\} \tag{C3}$$

To facilitate our analysis, note in tables 2, 4, and 7 that $\mathbf{X}_v$, the forward, first derivative matrix operator of $(2n-1)$th-order accuracy, may be rewritten as

$$\left({}^{(1)}\Delta^+_{(2n-1)}\right)_i = \left({}^{(1)}\Delta^c_{(2n)}\right)_i + \left\{\frac{[(n-1)!]}{\prod_{l=1}^{n}(4l-2)}\right\} \left({}^{(2n)}\Delta^c_{(2)}\right)_i \tag{C4}$$

where $\left({}^{(1)}\Delta^+_{(2n-1)}\right)_i$, $\left({}^{(1)}\Delta^c_{(2n)}\right)_i$, and $\left({}^{(2n)}\Delta^c_{(2)}\right)_i$ represent the explicit, forward, first derivative operator to $(2n-1)$th-order accuracy at grid point i; the explicit, centered, first derivative operator to $(2n)$th-order accuracy at grid point i; and the explicit, centered, $(2n)$th derivative operator to second-order accuracy at grid point i, respectively.

The matrix $\mathbf{X}$ may be considered by rewriting the finite-difference stencil of which it is composed

$$Ff_{i-3} + Df_{i-2} + Bf_{i-1} + Gf_i + Bf_{i+1} + Df_{i+2} + Ff_{i+3} \tag{C5}$$

as

$$F\left[\left({}^{(2)}\Delta^{c}_{(2)}\right)_{i+2} + \left({}^{(2)}\Delta^{c}_{(2)}\right)_{i-2}\right] + (D+2F)\left[\left({}^{(2)}\Delta^{c}_{(2)}\right)_{i+1} + \left({}^{(2)}\Delta^{c}_{(2)}\right)_{i-1}\right] + (B+2D+3F)\left({}^{(2)}\Delta^{c}_{(2)}\right)_{i} \tag{C6}$$

Although we do not utilize these results, for the special case of $B = -(4D+9F)$, the finite difference stencil in $\mathbf{X}$ is shown to be given by

$$F\left[\left({}^{(4)}\Delta^{c}_{(2)}\right)_{i+1} + \left({}^{(4)}\Delta^{c}_{(2)}\right)_{i-1}\right] + (D+4F)\left({}^{(4)}\Delta^{c}_{(2)}\right)_{i} \tag{C7}$$

where G is still given by $G = -2(B+D+F)$ or, in this particular case, $G = 2(3D+8F)$. By further enforcing $D = -6F$, equation (C7) becomes

$$F\left({}^{(6)}\Delta^{c}_{(2)}\right)_{i} \tag{C8}$$

and the stencil in $\mathbf{X}$ then represents the second-order accurate approximation to the sixth derivative.

The matrices $\mathbf{A}^{2n}, \mathbf{X}$, and $\mathbf{X}_v$ may be represented as

$$\left.\begin{aligned} \mathbf{A}^{2n} &= (\Delta x)\left\{\frac{\partial}{\partial x} + O\left[(\Delta x)^{2n}\right]\right\} \\ \mathbf{X} &\propto (\Delta x)^{2}\left\{\frac{\partial^{2}}{\partial x^{2}} + O\left[(\Delta x)^{2}\right]\right\} \\ \mathbf{X}_v &\propto (\Delta x)^{2n}\left\{\frac{\partial^{2n}}{\partial x^{2n}} + O\left[(\Delta x)^{2}\right]\right\} \end{aligned}\right\} \tag{C9}$$

The terms $\mathbf{A}^{2n}, \mathbf{X}$, and $\mathbf{X}_v$ that occur in both extended MacCormack and RKLW schemes are now given by

$$\left.\begin{aligned} \mathbf{A}^{2n} &\propto (\Delta x) \\ \mathbf{X} &\propto (\Delta x)^{2} \\ \mathbf{X}_v &\propto (\Delta x)^{2n} \end{aligned}\right\} \tag{C10}$$

Equations (C10) imply that

$$\left.\begin{aligned} \mathbf{Z}_1 &\propto (\Delta x)^{2} \\ \mathbf{Z}_2 &\propto (\Delta x)^{2n+1} \\ \mathbf{Z}_3 &\propto (\Delta x)^{3} \\ \mathbf{Z}_4 &\propto (\Delta x)^{2n+2} \end{aligned}\right\} \tag{C11}$$

Also note that $\mathbf{A}^{2n}, \mathbf{X}$, and $\mathbf{X}_v$ are antisymmetric, symmetric, and symmetric, respectively. Each symmetric matrix has identical diagonal elements; this implies that $\mathbf{Z}_1$ and $\mathbf{Z}_4$ are symmetric, $\mathbf{Z}_2$ and $\mathbf{Z}_3$ are antisymmetric, and therefore

$$\left.\begin{aligned} \mathbf{A}^{+}\mathbf{B}\mathbf{A}_v^{-}\mathbf{A}^{-}\mathbf{B}\mathbf{A}_v^{+} &= (\mathbf{Z}_1-\mathbf{Z}_4)^{2} - (\mathbf{Z}_2-\mathbf{Z}_3)^{2} + 2\left[\mathbf{Z}_1(\mathbf{Z}_3-\mathbf{Z}_2) - \mathbf{Z}_4(\mathbf{Z}_3+\mathbf{Z}_2)\right] \\ \mathbf{A}^{+}\mathbf{B}\mathbf{A}_v^{-} + \mathbf{A}^{-}\mathbf{B}\mathbf{A}_v^{+} &= 2(\mathbf{Z}_1-\mathbf{Z}_4) \end{aligned}\right\} \tag{C12}$$

The full RKLW scheme is written as

$$U^{n+1} = \Bigg(\mathbf{I} + \frac{4}{3}\beta_2\beta_1\lambda_v^{'}(\mathbf{I}+\lambda_v^{'}\mathbf{Z}_1)(\mathbf{Z}_1-\mathbf{Z}_4) + \frac{2}{3}\lambda_v^{'}\mathbf{Z}_1 + \frac{2}{3}\beta_2\beta_1^2\lambda_v^{'2}(\mathbf{I}+\lambda_v^{'}\mathbf{Z}_1)$$
$$\times \left\{(\mathbf{Z}_1-\mathbf{Z}_4)^2-(\mathbf{Z}_2-\mathbf{Z}_3)^2 + 2\left[\mathbf{Z}_1(\mathbf{Z}_3-\mathbf{Z}_2)-\mathbf{Z}_4(\mathbf{Z}_3+\mathbf{Z}_2)\right]\right\}\Bigg)U^n \tag{C13}$$

and the extended MacCormack schemes are given as

$$U^{n+1} = \Bigg(\mathbf{I} + \frac{\lambda_v^{'2}}{2}\left\{(\mathbf{Z}_1-\mathbf{Z}_4)^2-(\mathbf{Z}_2-\mathbf{Z}_3)^2 + 2\left[\mathbf{Z}_1(\mathbf{Z}_3-\mathbf{Z}_2)-\mathbf{Z}_4(\mathbf{Z}_3+\mathbf{Z}_2)\right]\right\}$$
$$+ \lambda_v^{'}(\mathbf{Z}_1-\mathbf{Z}_4)\Bigg)U^n \tag{C14}$$

With $\beta_1 = 1$ and $\beta_2 = \frac{1}{4}$, the RKLW schemes become

$$U^{n+1} = \Bigg(\mathbf{I} + \left(\lambda_v^{'}\mathbf{Z}_1\right) + \frac{1}{2}\left(\lambda_v^{'}\mathbf{Z}_1\right)^2 + \frac{1}{6}\left(\lambda_v^{'}\mathbf{Z}_1\right)^3 - \frac{1}{3}\lambda_v^{'}(1+\lambda_v^{'}\mathbf{Z}_1)\mathbf{Z}_4 - \frac{1}{6}\lambda_v^{'2}(1+\lambda_v^{'}\mathbf{Z}_1)$$
$$\times \left\{(\mathbf{Z}_3-\mathbf{Z}_2)^2-2\mathbf{Z}_1\mathbf{Z}_4+\mathbf{Z}_4^2+2\left[\mathbf{Z}_1(\mathbf{Z}_3-\mathbf{Z}_2)-\mathbf{Z}_4(\mathbf{Z}_3+\mathbf{Z}_2)\right]\right\}\Bigg)U^n \tag{C15}$$

and similarly, for the extended MacCormack schemes,

$$U^{n+1} = \Bigg(\mathbf{I} + \left(\lambda_v^{'}\mathbf{Z}_1\right) + \frac{1}{2}\left(\lambda_v^{'}\mathbf{Z}_1\right)^2 - \lambda_v^{'}\mathbf{Z}_4$$
$$- \frac{1}{2}\lambda_v^{'}\left\{(\mathbf{Z}_3-\mathbf{Z}_2)^2-2\mathbf{Z}_1\mathbf{Z}_4+\mathbf{Z}_4^2+2\left[\mathbf{Z}_1(\mathbf{Z}_3-\mathbf{Z}_2)-\mathbf{Z}_4(\mathbf{Z}_3+\mathbf{Z}_2)\right]\right\}\Bigg)U^n \tag{C16}$$

Making use of the following relations

$$\begin{aligned} U_t^n &= [b(x)U_x^n]_x \\ &= (\Delta x)^{-2}(\mathbf{A}^{2n}\mathbf{B}\mathbf{A}^{2n})U^n \\ &= (\Delta x)^{-2}(\mathbf{Z}_1)U^n \end{aligned} \tag{C17}$$

$$\begin{aligned} U_{tt}^n &= \{b(x)[b(x)U_x^n]_x\}_x \\ &= (\Delta x)^{-4}(\mathbf{A}^{2n}\mathbf{B}\mathbf{A}^{2n}\mathbf{A}^{2n}\mathbf{B}\mathbf{A}^{2n})U^n \\ &= (\Delta x)^{-4}(\mathbf{Z}_1\mathbf{Z}_1)U^n \end{aligned} \tag{C18}$$

$$\begin{aligned} U_{ttt}^n &= \left(b(x)\{b(x)[b(x)U_x^n]_x\}_x\right)_x \\ &= (\Delta x)^{-6}(\mathbf{A}^{2n}\mathbf{B}\mathbf{A}^{2n}\mathbf{A}^{2n}\mathbf{B}\mathbf{A}^{2n}\mathbf{A}^{2n}\mathbf{B}\mathbf{A}^{2n})U^n \\ &= (\Delta x)^{-6}(\mathbf{Z}_1\mathbf{Z}_1\mathbf{Z}_1)U^n \end{aligned} \tag{C19}$$

gives

$$U^{n+1} = U^n + (\Delta t)U_t^n + \frac{1}{2}(\Delta t)^2 U_{tt}^n + \frac{1}{6}(\Delta t)^3 U_{ttt}^n - \frac{1}{3}\lambda_v'(1+\lambda_v'\mathbf{Z}_1)\mathbf{Z}_4 - \frac{1}{6}\lambda_v'^2(1+\lambda_v'\mathbf{Z}_1)$$
$$\times \left\{(\mathbf{Z}_3-\mathbf{Z}_2)^2 - 2\mathbf{Z}_1\mathbf{Z}_4 + \mathbf{Z}_4^2 + 2\left[\mathbf{Z}_1(\mathbf{Z}_3-\mathbf{Z}_2) - \mathbf{Z}_4(\mathbf{Z}_3+\mathbf{Z}_2)\right]\right\} U^n \tag{C20}$$

for the RKLW schemes and

$$U^{n+1} = U^n + (\Delta t)U_t^n + \frac{1}{2}(\Delta t)^2 U_{tt}^n - \lambda_v'\mathbf{Z}_4$$
$$- \frac{1}{2}\lambda_v'^2\left\{(\mathbf{Z}_3-\mathbf{Z}_2)^2 - 2\mathbf{Z}_1\mathbf{Z}_4 + \mathbf{Z}_4^2 + 2\left[\mathbf{Z}_1(\mathbf{Z}_3-\mathbf{Z}_2) - \mathbf{Z}_4(\mathbf{Z}_3+\mathbf{Z}_2)\right]\right\} U^n \tag{C21}$$

for the extended MacCormack schemes.

The lowest order error terms present in the extended MacCormack scheme are those proportional to $\lambda_v'^2(\mathbf{Z}_3-\mathbf{Z}_2)^2$, $\lambda_v'^2\mathbf{Z}_1(\mathbf{Z}_3-\mathbf{Z}_2)$, and $\lambda_v'\mathbf{Z}_4$. These three terms have respective errors of $(\Delta t)^2(\Delta x)^2$, $(\Delta t)^2(\Delta x)$, and $(\Delta t)(\Delta x)^{2n}$ (n = 1). RKLW error terms are very similar with the term $(1+\lambda_v'\mathbf{Z}_1)$ being equal to $(1+\Delta t)$.

Both $\mathbf{Z}_2$ and $\mathbf{Z}_3$ are cross-coupling terms present in the extended MacCormack and RKLW schemes, and linear occurrences may be removed by a procedure discussed later in this appendix. Error terms that contain only $\mathbf{Z}_1$ and/or $\mathbf{Z}_4$ cannot be removed by this procedure. Therefore, the (3-2E) scheme does not retain formal accuracy. In cases of $n > 1$, the leading order error terms are $(\Delta t)^2(\Delta x)^2$ and $(\Delta t)(\Delta x)^{2n}$. All extended MacCormack and RKLW schemes except (3-2E) are formally accurate to their stated order in the absence of boundaries on the viscous problem.

We now consider the second part of the problem, namely

$$U_t + F_x = 0$$

where $F = F(U)$ and $F_x = F_U U_x = f U_x$. With no loss of generality, the term $[b(x)U_x]_x$ is absorbed into F_x. The RKLW schemes may be represented for the equation $U_t = -F_x$ as

$$\left.\begin{aligned} U^* &= (\mathbf{I} - \beta_1\lambda f^n\mathbf{A}^+)U^n \\ U^{**} &= (\mathbf{I} - \beta_1\lambda f^*\mathbf{A}^-)U^* \\ U^\# &= [U^n + \beta_2(U^{**} - U^n)] \\ U^{n+1} &= \frac{1}{3}[U^n + 2(\mathbf{I} - \lambda f^{**}\mathbf{A}^{2n})U^\#] \end{aligned}\right\} \tag{C22}$$

where, again, $\lambda = \frac{\Delta x}{\Delta t}$. With

$$\left.\begin{aligned} \mathbf{A}^{2n} f \mathbf{A}^{2n} &= \mathbf{Z}_5 \\ \mathbf{A}^{2n} f \mathbf{X} &= \mathbf{Z}_6 \\ \mathbf{X} f \mathbf{A}^{2n} &= \mathbf{Z}_7 \\ \mathbf{X} f \mathbf{X} &= \mathbf{Z}_8 \\ \mathbf{Z} &= \mathbf{Z}_5 + \mathbf{Z}_6 - \mathbf{Z}_7 - \mathbf{Z}_8 \end{aligned}\right\} \tag{C23}$$

the full RKLW scheme is written as

$$U^{n+1} = \Big(\mathbf{I} - \frac{2}{3}\lambda f^{**}\mathbf{A}^{2n}\beta_2\Big\{-\beta_1\lambda[(f^n+f^*)\mathbf{A}^{2n} + (f^n-f^*)\mathbf{X}] + \beta_1^2\lambda^2 f^*\mathbf{Z}\Big\}$$
$$- \frac{2}{3}\lambda f^{**}\mathbf{A}^{2n} + \frac{2}{3}\beta_2\Big\{-\beta_1\lambda[(f^n+f^*)\mathbf{A}^{2n} + (f^n-f^*)\mathbf{X}] + \beta_1^2\lambda^2 f^*\mathbf{Z}\Big\}\Big)U^n \tag{C24}$$

If we expand f^* and f^{**} in a Taylor series with the coefficients from the Butcher array for the RKLW scheme ($c_i = (0, 1, \frac{1}{2})$), then

$$f^* = f^n + (c_2\Delta t)f_t^n + \frac{(c_2\Delta t)^2}{2}f_{tt}^n + \cdots$$
$$= f^n + (\Delta t)f_t^n + \frac{(\Delta t)^2}{2}f_{tt}^n + \cdots \tag{C25}$$

$$f^{**} = f^n + (c_3\Delta t)f_t^n + \frac{(c_3\Delta t)^2}{2}f_{tt}^n + \cdots$$
$$= f^n + \frac{(\Delta t)}{2}f_t^n + \frac{(\Delta t)^2}{8}f_{tt}^n + \cdots \tag{C26}$$

The expansions for f^* are identical for the extended MacCormack and the RKLW schemes. Note that the error of the quantities $\mathbf{Z}_5, \mathbf{Z}_6, \mathbf{Z}_7$, and $\mathbf{Z}_8$ are proportional to $(\Delta x)^2$, $(\Delta x)^3$, $(\Delta x)^3$, and $(\Delta x)^4$, respectively. Inserting the values of β_1 and β_2 and expanding give

$$U^{n+1} = \Big[\mathbf{I} + \frac{1}{6}\lambda^2 f^{**}\mathbf{A}^{2n}(f^n+f^*)\mathbf{A}^{2n} + \frac{1}{6}\lambda^2 f^{**}\mathbf{A}^{2n}(f^n-f^*)\mathbf{X} - \frac{1}{6}\lambda^3 f^{**}\mathbf{A}^{2n}(f^n-f^*)\mathbf{Z}$$
$$- \frac{2}{3}\lambda f^{**}\mathbf{A}^{2n} - \frac{1}{6}\lambda(f^n+f^*)\mathbf{A}^{2n} - \frac{1}{6}\lambda(f^n-f^*)\mathbf{X} + \frac{1}{6}\lambda^2 f^*\mathbf{Z}\Big]U^n \tag{C27}$$

In addition,

$$U_t^n = -f^n U_x^n$$
$$= (\Delta x)^{-1}(-f^n\mathbf{A}^{2n})U^n \tag{C28}$$

$$U_{tt}^n = -f_t^n U_x^n + f^n(f^n U_x^n)_x$$
$$= (\Delta x)^{-2}(-f_t^n\mathbf{A}^{2n} + f^n\mathbf{A}^{2n}f^n\mathbf{A}^{2n})U^n \tag{C29}$$

$$U_{ttt}^n = -f_{tt}^n U_x^n + 2f_t^n(f^n U_x^n)_x + f^n(f_t^n U_x^n)_x - f^n[f^n(f^n U_x^n)_x]_x$$
$$= (\Delta x)^{-3}(-f_{tt}^n\mathbf{A}^{2n} + 2f_t^n\mathbf{A}^{2n}f^n\mathbf{A}^{2n} + f^n\mathbf{A}^{2n}f_t^n\mathbf{A}^{2n} - \mathbf{A}^{2n}f^n\mathbf{A}^{2n}f^n\mathbf{A}^{2n})U^n \tag{C30}$$

If we use equations (C28), (C29), and (C30) and neglect the terms with error proportional to $(\Delta t)^4$ and higher and cross-couple terms proportional to $(\Delta t)^l(\Delta x)^k$, where $l+k > 4$ and higher, then after significant manipulation, RKLW schemes are

$$
\begin{aligned}
U^{n+1} = U^n \; + \; (\Delta t) U_t^n \; + \; \frac{1}{2}(\Delta t)^2 U_{tt}^n \; + \; \frac{1}{6}(\Delta t)^3 U_{ttt}^n \\
+ \; \left[\frac{\lambda(\Delta t)}{6} f_t^n \mathbf{X} \; + \; \frac{\lambda^2}{6} f^n (\mathbf{A}^{2n} f \mathbf{X} - \mathbf{X} f \mathbf{A}^{2n}) \right] U^n \\
+ \; \left[\frac{\lambda(\Delta t)^2}{12} f_{tt}^n \mathbf{X} \; - \; \frac{\lambda^2(\Delta t)}{6} \mathbf{A}^{2n} f^n \mathbf{X} \; + \; \frac{\lambda^2(\Delta t)}{6} f_t^n (\mathbf{A}^{2n} f \mathbf{X} - \mathbf{X} f \mathbf{A}^{2n}) \right] U^n \\
+ \; \left[\frac{\lambda^2}{6} \mathbf{X} f^n \mathbf{X} \right] U^n
\end{aligned}
\tag{C31}
$$

The terms in brackets have an error that is proportional to $(\Delta t)^2(\Delta x)$, $(\Delta t)^3(\Delta x)$, and $(\Delta t)^2(\Delta x)^2$, respectively; the first group must be removed in order to retain the formal accuracy of the scheme on the nonlinear problem. Ideally, all other error terms listed should also be removed. For the linear problem, $f_t^n = f_{tt}^n = 0$ and $\mathbf{A}^{2n} f \mathbf{X} = \mathbf{X} f \mathbf{A}^{2n}$; the scheme is formally (3-[2n])th-order accurate, with the highest error contributed by the term $\frac{\lambda^2}{6}(\mathbf{X} f^n \mathbf{X}) U^n$. For the nonlinear problem, the step from time level $(n+1)$ to $(n+2)$ is slightly different from the step from time level (n) to $(n+1)$. Let $\mathbf{F}$, $\mathbf{B}$, and $\mathbf{C}$ denote forward, backward, and centered differencing, respectively. Until this point, consideration has only been given to the RKLW scheme where the sequence of forward-backward-centered operations are repeated indefinitely: **F-B-C,** $\cdots$. If this sequence were modified to be **F-B-C, B-F-C,** $\cdots$, then each term for which the error is proportional to $(\Delta t)^2(\Delta x)$ and $(\Delta t)^3(\Delta x)$ vanishes. The term $\frac{\lambda^2}{6}(\mathbf{X} f^n \mathbf{X}) U^n$ still remains with an error proportional to $(\Delta t)^2(\Delta x)^2$. If the forward and backward operators are not permutated, the cross-coupling terms would remain and the scheme would be formally (2-[2n])th-order accurate.

The full, extended MacCormack scheme is written as

$$
U^{n+1} \; = \; \left\{ \mathbf{I} \; - \; \frac{\lambda}{2}[(f^* + f^n)\mathbf{A}^{2n} \; + \; (f^n - f^*)\mathbf{X}] + \; \frac{\lambda f^*}{2} \mathbf{Z} \right\} U^n \tag{C32}
$$

or

$$
\begin{aligned}
U^{n+1} = U^n \; + \; (\Delta t) U_t^n \; + \; \frac{1}{2}(\Delta t)^2 U_{tt}^n \; + \; \left[\frac{\lambda(\Delta t)}{2} f_t^n \mathbf{X} \; + \; \frac{\lambda^2}{6} f^n (\mathbf{A}^{2n} f \mathbf{X} - \mathbf{X} f \mathbf{A}^{2n}) \right] U^n \\
+ \; \left[\frac{\lambda^2}{6} \mathbf{X} f^n \mathbf{X} \right] U^n
\end{aligned}
\tag{C33}
$$

Again, the two terms in the first set of brackets of equation (C33) are proportional to $(\Delta t)^2(\Delta x)$ and may be removed by implementing the scheme as an **F-B, B-F,** $\cdots$ sequence. The error terms in the first set of brackets disappear for the linear problem and for the nonlinear problem with permutated operators, which leaves the last error term in the second set of brackets with an error proportional to $(\Delta t)^2(\Delta x)^2$. In multidimensions, this permutation would be implemented as

$$
\mathbf{F}_x \mathbf{F}_y - \mathbf{B}_x \mathbf{B}_y, \mathbf{B}_x \mathbf{B}_y - \mathbf{F}_x \mathbf{F}_y, \mathbf{F}_x \mathbf{B}_y - \mathbf{B}_x \mathbf{F}_y, \mathbf{B}_x \mathbf{F}_y - \mathbf{F}_x \mathbf{B}_y, \cdots
$$

for the extended MacCormack schemes and

$$
\mathbf{F}_x \mathbf{F}_y - \mathbf{B}_x \mathbf{B}_y - \mathbf{C}_x \mathbf{C}_y, \mathbf{B}_x \mathbf{B}_y - \mathbf{F}_x \mathbf{F}_y - \mathbf{C}_x \mathbf{C}_y, \mathbf{F}_x \mathbf{B}_y - \mathbf{B}_x \mathbf{F}_y - \mathbf{C}_x \mathbf{C}_y, \mathbf{B}_x \mathbf{F}_y - \mathbf{F}_x \mathbf{B}_y - \mathbf{C}_x \mathbf{C}_y, \cdots
$$

for the RKLW scheme. In the present computations, we found it sufficient to only implement the RKLW scheme as

$$\mathbf{F}_x\mathbf{F}_y - \mathbf{B}_x\mathbf{B}_y - \mathbf{C}_x\mathbf{C}_y, \mathbf{B}_x\mathbf{B}_y - \mathbf{F}_x\mathbf{F}_y - \mathbf{C}_x\mathbf{C}_y, \cdots$$

and the extended MacCormack scheme as

$$\mathbf{F}_x\mathbf{F}_y - \mathbf{B}_x\mathbf{B}_y, \mathbf{B}_x\mathbf{B}_y - \mathbf{F}_x\mathbf{F}_y, \cdots$$

A discussion of multidimensional stability for finite-difference schemes can be found in the work of Beckers. (See ref. 59.)

This analysis does not need to be performed for the Runge-Kutta central-difference schemes because the spatial and temporal accuracies are not coupled in the numerical scheme; therefore, each scheme retains its respective formal accuracy for the nonlinear problem.

Further work might include replacing $\mathbf{X}$ with a stencil having an error that is proportional to $(\Delta x)^4$. Using forward and backward differences with different weightings on all three stages of the RKLW scheme might minimize error terms.

Appendix D

Higher Order Boundary Treatments

When eighth-order spatially accurate, central-difference stencils are coupled with either third- or fourth-order temporally accurate Runge-Kutta schemes, seventh-order accurate stable boundary stencils for the explicit eighth-order accurate spatial derivative operator result and are given by

$$\begin{aligned} f_1' = \frac{1}{105000\Delta x}(&-375150f_1 + 1565172f_2 - 4039140f_3 + 7180075f_4 \\ &- 8503950f_5 + 6676740f_6 - 3378844f_7 + 1024890f_8 \\ &- 157500f_9 + 8400f_{10} - 840f_{11} + 147f_{12}) \end{aligned} \tag{D1}$$

$$\begin{aligned} f_2' = \frac{1}{105000\Delta x}(&56400f_1 - 725676f_2 + 2331945f_3 - 4322850f_4 \\ &+ 5296900f_5 - 4232970f_6 + 2147502f_7 - 641320f_8 \\ &+ 94500f_9 - 5250f_{10} + 945f_{11} - 126f_{12}) \end{aligned} \tag{D2}$$

$$\begin{aligned} f_3' = \frac{1}{21000\Delta x}(&8186f_1 - 66262f_2 + 181370f_3 - 336385f_4 \\ &+ 407120f_5 - 289352f_6 + 114674f_7 - 18070f_8 \\ &- 1890f_9 + 630f_{10} - 84f_{11} + 63f_{12}) \end{aligned} \tag{D3}$$

$$\begin{aligned} f_4' = \frac{1}{210000\Delta x}(&16480f_1 - 121338f_2 + 348810f_3 - 944475f_4 \\ &+ 1234800f_5 - 792120f_6 + 323876f_7 - 77310f_8 \\ &+ 16800f_9 - 7350f_{10} + 1890f_{11} - 63f_{12}) \end{aligned} \tag{D4}$$

For the tridiagonal eighth-order accurate derivative operator, the boundary stencils are given by

$$\begin{aligned} f_1' = \frac{1}{21000\Delta x}(&-127530f_1 + 738864f_2 - 2323230f_3 + 4529525f_4 \\ &- 5668950f_5 + 4618740f_6 - 2394728f_7 + 730230f_8 \\ &- 105000f_9 + 2100f_{10} - 210f_{11} + 189f_{12}) \end{aligned} \tag{D5}$$

$$\begin{aligned} f_2' = \frac{1}{21000\Delta x}(&18504f_1 - 201936f_2 + 660765f_3 - 1241625f_4 \\ &+ 1510460f_5 - 1183518f_6 + 578382f_7 - 159890f_8 \\ &+ 18900f_9 - 210f_{10} + 189f_{11} - 21f_{12}) \end{aligned} \tag{D6}$$

$$f_3' = \frac{1}{210000\Delta x}(99920f_1 - 818104f_2 + 2402330f_3 - 4643275f_4$$
$$+ 5814200f_5 - 4407620f_6 + 1947008f_7 - 391330f_8$$
$$- 21000f_9 + 18900f_{10} - 1050f_{11} + 21f_{12}) \tag{D7}$$

$$f_4' = \frac{1}{210000\Delta x}(5140f_1 - 36246f_2 + 74970f_3 - 456225f_4$$
$$+ 718200f_5 - 474600f_6 + 225092f_7 - 65970f_8$$
$$+ 10500f_9 - 1050f_{10} + 210f_{11} - 21f_{12}) \tag{D8}$$

and for the compact pentadiagonal eighth-order accurate derivative operator, by

$$f_1' = \frac{1}{84000\Delta x}(-556152f_1 + 3316908f_2 - 10530450f_3 + 20529425f_4$$
$$- 25599000f_5 + 20734644f_6 - 10674356f_7 + 3236550f_8$$
$$- 470400f_9 + 12600f_{10} - 42f_{11} + 273f_{12}) \tag{D9}$$

$$f_2' = \frac{1}{105000\Delta x}(99660f_1 - 1065099f_2 + 3490410f_3 - 6562500f_4$$
$$+ 7964320f_5 - 6213060f_6 + 3014508f_7 - 822760f_8$$
$$+ 94500f_9 - 945f_{10} + 1050f_{11} - 84f_{12}) \tag{D10}$$

$$f_3' = \frac{1}{210000\Delta x}(99920f_1 - 818104f_2 + 2402330f_3 - 4643275f_4$$
$$+ 5814200f_5 - 4407620f_6 + 1947008f_7 - 391330f_8$$
$$- 21000f_9 + 18900f_{10} - 1050f_{11} + 21f_{12}) \tag{D11}$$

$$f_4' = \frac{1}{210000\Delta x}(-1580f_1 + 17136f_2 - 110670f_3 - 86625f_4$$
$$+ 256200f_5 - 101220f_6 + 32228f_7 - 6330f_8$$
$$+ 2100f_9 - 2100f_{10} + 1050f_{11} - 189f_{12}) \tag{D12}$$

Each of these expressions is denoted by $7^4, 7^4, 7^4, 7^4$-8-$7^4, 7^4, 7^4, 7^4$ schemes and is formally eighth-order accurate in space. We were not able to find stable, accuracy-preserving numerical boundary conditions for the eighth-order spatially accurate dissipative schemes.

Seventh-order accurate boundary stencils for the seventh-order viscous operator used in the eighth-order extended MacCormack and RKLW schemes are

$$f_1' = \frac{1}{420\Delta x}(-1089f_1 + 2940f_2 - 4410f_3 + 4900f_4$$
$$- 3675f_5 + 1764f_6 - 490f_7 + 60f_8) \tag{D13}$$

$$f_2' = \frac{1}{420\Delta x}(-60f_1 - 609f_2 + 1260f_3 - 1050f_4 + 700f_5 - 315f_6 + 84f_7 - 10f_8) \tag{D14}$$

$$f_3' = \frac{1}{420\Delta x}(+10f_1 - 140f_2 - 329f_3 + 700f_4 - 350f_5 + 140f_6 - 35f_7 + 4f_8) \tag{D15}$$

The values of f_4' on the backward step and f_{nx-3}' on the forward step are closed by using the seventh-order viscous interior stencil and the negative of its complex conjugate (in Fourier space), respectively. For the tenth-order spatially accurate Runge-Kutta schemes given in table 4, ninth-order accurate stable boundary stencils for the central and dissipative stencils were derived but were subject to severe CFL restrictions; hence, these are not presented.

These boundaries may be closed to lower order also. Explicit stencils may be closed as $(3, 3, 4, x, y\text{-}10\text{-}y, x, 4, 3, 3)$, where x is either the fourth- or sixth-order accurate explicit stencil and y is either the fourth-, sixth-, or eighth-order accurate explicit stencil. Tridiagonal stencils may be implemented as $(3, 4, x, y\text{-}10\text{-}y, x, 4, 3)$, where x is the fourth- or sixth-order accurate tridiagonal stencil and y is either the fourth-, sixth-, or eighth-order accurate tridiagonal stencils. The pentadiagonal stencil is closed with $(3, 4, x\text{-}10\text{-}x, 4, 3)$, where x is either a sixth-order accurate tridiagonal or an eighth-order accurate pentadiagonal stencil. Each of these lower order closures results in a formally spatially fourth-order scheme. Other closures not mentioned may also be constructed.

The viscous boundaries for the (3-10P) RKLW scheme are closed with the following ninth-order stencils:

$$f_1' = \frac{1}{2520\Delta x}(-7129f_1 + 22680f_2 - 45360f_3 + 70560f_4 - 79380f_5 + 63504f_6 - 35280f_7 + 12960f_8 - 2835f_9 + 280f_{10}) \tag{D16}$$

$$f_2' = \frac{1}{2520\Delta x}(-280f_1 - 4329f_2 + 10080f_3 - 11760f_4 + 11760f_5 - 8820f_6 + 4704f_7 - 1680f_8 + 360f_9 - 35f_{10}) \tag{D17}$$

$$f_3' = \frac{1}{2520\Delta x}(+35f_1 - 630f_2 - 2754f_3 + 5880f_4 - 4410f_5 + 2940f_6 - 1470f_7 + 504f_8 - 105f_9 + 10f_{10}) \tag{D18}$$

$$f_4' = \frac{1}{2520\Delta x}(-10f_1 + 135f_2 - 1080f_3 - 1554f_4 + 3780f_5 - 1890f_6 + 840f_7 - 270f_8 + 54f_9 - 5f_{10}) \tag{D19}$$

The values of f_5' on the backward step and f_{nx-4}' on the forward step are closed by using the ninth-order viscous interior stencil and the negative of its complex conjugate (in Fourier space), respectively.

Appendix E

Explicit Finite-Difference Filters

To filter the vector $\mathbf{U}$, the dissipation matrix $\mathbf{D}$ must be specified, including boundary points. Coefficients for the interior portion have already been given in table 7 and should be familiar as elements of Pascal's triangle. The boundary portions (upper left portion of $\mathbf{D}$) of the dissipation matrix are given for filters of orders two through twenty in the interior and orders one through ten at the boundary. The lower right portion of $\mathbf{D}$ on a grid of N_x points is given by $D_{i,j} = D_{N_x+1-i,N_x+1-j}$. To clarify the information presented, the full dissipation matrix is written out for the second-order filter and its first-order boundary points as

$$\begin{bmatrix} +1 & -1 & 0 & 0 & 0 & 0 \\ -1 & +2 & -1 & 0 & 0 & 0 \\ 0 & -1 & +2 & -1 & 0 & 0 \\ 0 & 0 & -1 & +2 & -1 & 0 \\ 0 & 0 & 0 & -1 & +2 & -1 \\ 0 & 0 & 0 & 0 & -1 & +1 \end{bmatrix} \tag{E1}$$

Boundary points for the second-order dissipation matrix $\mathbf{D}$ are

$$\begin{bmatrix} +1 & -1 \\ -1 & +2 \end{bmatrix} \tag{E2}$$

The lower row and the right column are the interior operator. Similarly, the full dissipation matrix can be constructed for the fourth-order filter with

$$\begin{bmatrix} -1 & +2 & -1 \\ +2 & -5 & +4 \\ -1 & +4 & -6 \end{bmatrix} \tag{E3}$$

for sixth order with

$$\begin{bmatrix} +1 & -3 & +3 & -1 \\ -3 & +10 & -12 & +6 \\ +3 & -12 & +19 & -15 \\ -1 & +6 & -15 & +20 \end{bmatrix} \tag{E4}$$

for eighth order with

$$\begin{bmatrix} -1 & +4 & -6 & +4 & -1 \\ +4 & -17 & +28 & -22 & +8 \\ -6 & +28 & -53 & +52 & -28 \\ +4 & -22 & +52 & -69 & +56 \\ -1 & +8 & -28 & +56 & -70 \end{bmatrix} \tag{E5}$$

for tenth order with

$$\begin{bmatrix} +1 & -5 & +10 & -10 & +5 & -1 \\ -5 & +26 & -55 & +60 & -35 & +10 \\ +10 & -55 & +126 & -155 & +110 & -45 \\ -10 & +60 & -155 & +226 & -205 & +120 \\ +5 & -35 & +110 & -205 & +251 & -210 \\ -1 & +10 & -45 & +120 & -210 & +252 \end{bmatrix} \tag{E6}$$

for twelfth order with

$$\begin{bmatrix} -1 & +6 & -15 & +20 & -15 & +6 & -1 \\ +6 & -37 & +96 & -135 & +110 & -51 & +12 \\ -15 & +96 & -262 & +396 & -360 & +200 & -66 \\ +20 & -135 & +396 & -662 & +696 & -480 & +220 \\ -15 & +110 & -360 & +696 & -887 & +786 & -495 \\ +6 & -51 & +200 & -480 & +786 & -923 & +792 \\ -1 & +12 & -66 & +220 & -495 & +792 & -924 \end{bmatrix} \tag{E7}$$

for fourteenth order with

$$\begin{bmatrix} +1 & -7 & +21 & -35 & +35 & -21 & +7 & -1 \\ -7 & +50 & -154 & +266 & -280 & +182 & -70 & +14 \\ +21 & -154 & +491 & -889 & +1001 & -721 & +329 & -91 \\ -35 & +266 & -889 & +1716 & -2114 & +1736 & -966 & +364 \\ +35 & -280 & +1001 & -2114 & +2941 & -2849 & +1981 & -1001 \\ -21 & +182 & -721 & +1736 & -2849 & +3382 & -2996 & +2002 \\ +7 & -70 & +329 & -966 & +1981 & -2996 & +3431 & -3003 \\ -1 & +14 & -91 & +364 & -1001 & +2002 & -3003 & +3432 \end{bmatrix} \tag{E8}$$

for sixteenth order with

$$\begin{bmatrix} -1 & +8 & -28 & +56 & -70 & +56 & -28 & +8 & -1 \\ +8 & -65 & +232 & -476 & +616 & -518 & +280 & -92 & +16 \\ -28 & +232 & -849 & +1800 & -2436 & +2184 & -1302 & +504 & -120 \\ +56 & -476 & +1800 & -3985 & +5720 & -5572 & +3752 & -1750 & +560 \\ -70 & +616 & -2436 & +5720 & -8885 & +9640 & -7532 & +4312 & -1820 \\ +56 & -518 & +2184 & -5572 & +9640 & -12021 & +11208 & -7980 & +4368 \\ -28 & +280 & -1302 & +3752 & -7532 & +11208 & -12085 & +11432 & -8008 \\ +8 & -92 & +504 & -1750 & +4312 & -7980 & +11432 & -12869 & +11440 \\ -1 & +16 & -120 & +560 & -1820 & +4368 & -8008 & +11440 & -12870 \end{bmatrix} \tag{E9}$$

for eighteenth order with

$$\begin{bmatrix} +1 & -9 & +36 & -84 & +126 & -126 & +84 & -36 & +9 & -1 \\ -9 & +82 & -333 & +792 & -1218 & +1260 & -882 & +408 & -117 & +18 \\ +36 & -333 & +1378 & -3357 & +5328 & -5754 & +4284 & -2178 & +732 & -153 \\ -84 & +792 & -3357 & +8434 & -13941 & +15912 & -12810 & +7308 & -2934 & +816 \\ +126 & -1218 & +5328 & -13941 & +24310 & -29817 & +26496 & -17346 & +8442 & -3060 \\ -126 & +1260 & -5754 & +15912 & -29817 & +40186 & -40401 & +31032 & -18480 & +8568 \\ +84 & -882 & +4284 & -12810 & +26496 & -40401 & +47242 & -43425 & +31788 & -18564 \\ -36 & +408 & -2178 & +7308 & -17346 & +31032 & -43425 & +48538 & -43749 & +31824 \\ +9 & -117 & +732 & -2934 & +8442 & -18480 & +31788 & -43749 & +48619 & -43758 \\ -1 & +18 & -153 & +816 & -3060 & +8568 & -18564 & +31824 & -43758 & +48620 \end{bmatrix} \tag{E10}$$

and for twentieth order with

$$\begin{bmatrix}
-1 & +10 & -45 & +120 & -210 & +252 & -210 & +120 & -45 & +10 & -1 \\
+10 & -101 & +460 & -1245 & +2220 & -2730 & +2352 & -1410 & +570 & -145 & +20 \\
-45 & +460 & -2126 & +5860 & -10695 & +13560 & -12180 & +7752 & -3435 & +1020 & -190 \\
+120 & -1245 & +5860 & -16526 & +31060 & -40935 & +38760 & -26580 & +13152 & -4635 & +1140 \\
-210 & +2220 & -10695 & +31060 & -60626 & +83980 & -85035 & +63960 & -36030 & +15252 & -4845 \\
+252 & -2730 & +13560 & -40935 & +83980 & -124130 & +136900 & -115275 & +75300 & -38550 & +15504 \\
-210 & +2352 & -12180 & +38760 & -85035 & +136900 & -168230 & +162100 & -124725 & +77400 & -38760 \\
+120 & -1410 & +7752 & -26580 & +63960 & -115275 & +162100 & -182630 & +167500 & -125925 & +77520 \\
-45 & +570 & -3435 & +13152 & -36030 & +75300 & -124725 & +167500 & -184655 & +167950 & -125970 \\
+10 & -145 & +1020 & -4635 & +15252 & -38550 & +77400 & -125925 & +167950 & -184755 & +167960 \\
-1 & +20 & -190 & +1140 & -4845 & +15504 & -38760 & +77520 & -125970 & +167960 & -184756
\end{bmatrix} \tag{E11}$$

Each of these groups of boundary stencils representing $\frac{\partial^n U}{\partial x^n}$ to second-order accuracy has a very predictable pattern in Fourier space with coefficients that appear in Pascal's triangle.

References

1. Kennedy, Christopher A.; and Gatski, Thomas B.: Self-Similar Supersonic Variable-Density Shear Layers in Binary Systems. *Phys. Fluids*, vol. 6, no. 2, Feb. 1994, pp. 662–673.

2. Ninnemann, T. A.; and Ng, W. F.: A Concentration Probe for the Study of Mixing in Supersonic Shear Flows. *Exp. Fluids*, vol. 13, no. 2–3, 1992, pp. 98–104.

3. Soetrisno, Moeljo; Eberhardt, Scott; Riley, James J.; and McMurtry, Patrick: A Study of Inviscid, Supersonic Mixing Layers Using a Second-Order TVD Scheme. *A Collection of Technical Papers, Part 2—AIAA/ASME/SIAM/APS 1st National Fluid Dynamics Congress*, July 1988, pp. 1087–1094. (Available as AIAA-88-3676-CP.)

4. Yamamoto, S.; and Daiguji, H.: Higher-Order-Accurate Upwind Schemes for Solving the Compressible Euler and Navier-Stokes Equations. *Comput. & Fluids*, vol. 22, nos. 2/3, Mar.–May 1993, pp. 259–270.

5. Shu, Chi-Wang; Zang, Thomas A.; Erlebacher, Gordon; Whitaker, David; and Osher, Stanley: High-Order ENO Schemes Applied to Two- and Three-Dimensional Compressible Flow. *Appl. Numer. Math.*, vol. 9, 1992, pp. 45–71.

6. Grinstein, F. F.; and Kailasanath, K.: Compressibility, Exothermicity, and Three Dimensionality in Spatially Evolving Reactive Shear Flows. *13th International Colloquium on Dynamics of Explosions and Reactive Systems*, A. L. Kuhl, et al., eds., AIAA, 1993, pp. 413–436.

7. Rai, Man Mohan; and Moin, Parviz: Direct Numerical Simulation of Transition and Turbulence in a Spatially Evolving Boundary Layer. *A Collection of Technical Papers—AIAA 10th Computational Fluid Dynamics Conference*, June 1991, pp. 890–914. (Available as AIAA-91-1607-CP.)

8. Mukunda, H. D.; Sekar, B.; Carpenter, M. H.; Drummond, J. Philip; and Kumar, Ajay: *Direct Simulation of High-Speed Mixing Layers*. NASA TP-3186, 1992.

9. Gottlieb, David; and Turkel, Eli: Dissipative Two-Four Methods for Time-Dependent Problems. *Math. Comput.*, vol. 30, no. 136, Oct. 1976, pp. 703–723.

10. MacCormack, Robert W.: The Effect of Viscosity in Hypervelocity Impact Cratering. AIAA-69-354, Apr.–May 1969.

11. Carpenter, M. H.: A High-Order Compact Numerical Algorithm for Supersonic Flow. *Twelfth International Conference on Numerical Methods in Fluid Dynamics*, K. W. Morton, ed., Volume 371 of *Lecture Notes in Physics*, Springer-Verlag, 1990, pp. 254–258.

12. Lele, Sanjiva K.: Direct Numerical Simulation of Compressible Free Shear Flows. AIAA-89-0374, Jan. 1989.

13. Lele, Sanjiva K.: Compact Finite Difference Schemes With Spectral-Like Resolution. *J. Comput. Phys.*, vol. 103, 1992, pp. 16–42.

14. Sandham, N. D.; and Reynolds, W. C.: Three-Dimensional Simulations of Large Eddies in the Compressible Mixing Layer. *J. Fluid Mech.*, vol. 224, 1991, pp. 133–158.

15. Guillard, H.; Malé, J. M.; and Peyret, R.: Adaptive Spectral Methods With Application to Mixing Layer Computations. *J. Comput. Phys.*, vol. 102, no. 1, Sept. 1992, pp. 114–127.

16. Carpenter, Mark H.; Gottlieb, David; and Abarbanel, Saul: Stable and Accurate Boundary Treatments for Compact, High-Order Finite-Difference Schemes. *Appl. Numer. Math.*, vol. 12, 1993, pp. 55–87.

17. Purser, R. James: Notes—The Filtering of Meteorological Fields. *J. Climate & Appl. Meteorol.*, vol. 26, 1987, pp. 1764–1769.

18. Pulliam, Thomas H.: Artificial Dissipation Models for the Euler Equations. *AIAA J.*, vol. 24, no. 12, Dec. 1986, pp. 1931–1940.

19. Eriksson, Lars E.; and Rizzi, Arthur: Computer-Aided Analysis of the Convergence to Steady State of Discrete Approximations to the Euler Equations. *J. Comput. Phys.*, vol. 57, 1985, pp. 90–128.

20. Rusanov, V. V.: On Difference Schemes of Third Order Accuracy for Nonlinear Hyperbolic Systems. *J. Comput. Phys.*, vol. 5, no. 3, 1970, pp. 507–516.

21. Kutler, Paul; Lomax, Harvard; and Warming, R. F.: Computation of Space Shuttle Flow Fields Using Noncentered Finite-Difference Schemes. AIAA-72-193, Jan. 1972.

22. Kutler, Paul; Warming, R. F.; and Lomax, Harvard: Computation of Space Shuttle Flowfields Using Noncentered Finite-Difference Schemes. *AIAA J.*, vol. 11, no. 2, Feb. 1973, pp. 196–204.

23. Warming, R. F.; Kutler, Paul; and Lomax, Harvard: Second- and Third-Order Noncentered Difference Schemes for Nonlinear Hyperbolic Equations. *AIAA J.*, vol. 11, no. 2, 1973, pp. 189–196.

24. Drummond, J. Philip: *A Two-Dimensional Numerical Simulation of a Supersonic, Chemically Reacting Mixing Layer.* NASA TM-4055, 1988.

25. Strikwerda, John C.: *Finite Difference Schemes and Partial Differential Equations.* Wadsworth & Brooks/Cole Advanced Books & Software, 1989.

26. Anderson, Dale A.; Tannehill, John C.; and Pletcher, Richard H.: *Computational Fluid Mechanics and Heat Transfer.* Hemisphere Publ. Corp., 1984.

27. Hirsch, Charles: *Numerical Computation of Internal and Eternal Flows. Volume I—Fundamentals of Numerical Discretization.* John Wiley & Sons Ltd., 1988.

28. Yanenko, N. N.; Fedotova, Z. I.; Tusheva, L. A.; and Shokin, Yu. I.: Classification of Difference Schemes of Gas Dynamics by the Method of Differential Approximation—I One-Dimensional Case. *Comput. & Fluids*, vol. 11, no. 3, 1983, pp. 187–206.

29. Yanenko, N. N.; Fedotova, Z. I.; Kompaniets, L. A.; and Shokin, Yu. I.: Classification of Difference Schemes of Gas Dynamics by the Method of Differential Approximation—II Two-Dimensional Case. *Comput. & Fluids*, vol. 12, no. 2, 1984, pp. 93–121.

30. Hatay, Ferhat; and Biringen, Sedat: Direct Numerical Simulation of High-Speed Compressible Rotating Couette Flow. *Transitional and Turbulent Compressible Flows 1993*, L. D. Kral and T. A. Zang, eds., FED-Vol. 151, ASME, June 1993, pp. 93–99.

31. Eißler, W.; and Bestek, H.: Spatial Numerical Simulations of Nonlinear Transition Phenomena in Supersonic Boundary Layers. *Transitional and Turbulent Compressible Flows 1993*, L. D. Kral and T. A. Zang, eds., FED-Vol. 151, ASME, June 1993, pp. 69–76.

32. Normand, Xavier; and Lesieur, Marcel: Direct and Large-Eddy Simulations of Transition in the Compressible Boundary Layer. *Theor. Comput. Fluid Dyn.*, vol. 3, 1992, pp. 231–252.

33. Bayliss, Alvin; Parikh, Paresh; Maestrello, Lucio; and Turkel, Eli: *A Fourth-Order Scheme for the Unsteady Compressible Navier-Stokes Equations.* NASA CR-177994, ICASE Rep. No. 85-44, 1985.

34. Burstein, Samuel Z.; and Mirin, Arthur A.: Third Order Difference Methods for Hyperbolic Equations. *J. Comput. Phys.*, vol. 5, 1970, pp. 547–571.

35. Anderson, D. A.: A Comparison of Numerical Solutions to the Inviscid Equations of Fluid Motion. *J. Comput. Phys.*, vol. 15, May 1974, pp. 1–20.

36. Anderson, Dale; and Fattahi, Behrooz: A Comparison of Numerical Solutions of the Advective Equation. *J. Atmos. Sci.*, vol. 31, Sept. 1974, pp. 1500–1506.

37. Huang, Ching-Yuang; and Raman, Sethu: A Comparative Study of Numerical Advection Schemes Featuring a One-Step Modified WKL Algorithm. *Mon. Weather Rev.*, vol. 119, Dec. 1991, pp. 2900–2918.

38. Sun, Wen-Yih: Comments on "A Comparative Study of Numerical Advection Schemes Featuring a One-Step Modified WKL Algorithm." *Mon. Weather Rev.*, vol. 121, no. 1, Jan. 1993, pp. 310–311.

39. Abarbanel, S.; Gottlieb, D.; and Turkel, E.: Difference Schemes With Fourth Order Accuracy for Hyperbolic Equations. *SIAM J. Appl. Math.*, vol. 29, no. 2, Sept. 1975, pp. 329–351.

40. Turkel, E.; Abarbanel, S.; and Gottlieb, D.: Multidimensional Difference Schemes With Fourth-Order Accuracy. *J. Comput. Phys.*, vol. 21, 1976, pp. 85–113.

41. Reddy, A. Sivasankara: Higher Order Accuracy Finite-Difference Schemes for Hyperbolic Conservation Laws. *Int. J. Numer. Meth ods Eng.*, vol. 18, July 1982, pp. 1019–1029.

42. Lambert, J. D.: *Numerical Methods for Ordinary Differential Systems: The Initial Value Problem.* John Wiley & Sons Ltd., 1991.

43. Williamson, J. H.: Low-Storage Runge-Kutta Schemes. *J. Comput. Phys.*, vol. 35, no. 1, Mar. 15, 1980, pp. 48–56.

44. Pruett, C. D.; and Zang, T. A.: Direct Numerical Simulation of Laminar Breakdown in High-Speed, Axisymmetric Boundary Layers. *Theor. Comput. Fluid Dyn.*, vol. 3, 1992, pp. 345–367.

45. Erlebacher, Gordon; Hussaini, M. Y.; Kreiss, H. O.; and Sarkar, S.: The Analysis and Simulation of Compressible Turbulence. *Theor. Comput. & Fluid Dyn.*, vol. 2, no. 2, 1990, pp. 73–95.

46. Sowa, Johan: Stability of a Runge-Kutta Method for the Navier-Stokes Equation. *BIT*, vol. 30, 1990, pp. 542–560.

47. Warming, R. F.; and Hyett, B. J.: The Modified Equation Approach to the Stability and Accuracy Analysis of Finite-Difference Methods. *J. Comput. Phys.*, vol. 14, 1974, pp. 159–179.

48. Chang, Sin-Chung: On the Validity of the Modified Equation Approach to the Stability Analysis of Finite-Difference Methods. *Technical Papers—8th AIAA Computational Fluid Dynamics Conference*, June 1987, pp. 210–229. (Available as AIAA-87-1120.)

49. Van Leer, Bram: *Numerical Fluid Dynamics II.* ICASE Internal Rep. Doc. No. 36, Aug. 26, 1987.

50. Gustafsson, Bertil: The Convergence Rate for Difference Approximations to Mixed Initial Boundary Value Problems. *Math. Comput.*, vol. 29, no. 130, Apr. 1975, pp. 396–406.

51. Carpenter, Mark H.; Gottlieb, David; and Abarbanel, Saul: *Time-Stable Boundary Conditions for Finite-Difference Schemes Solving Hyperbolic Systems: Methodology and Application to High-Order Compact Schemes.* NASA CR-191436, ICASE Rep. No. 93-9, 1993.

52. Carpenter, Mark H.; Gottlieb, David; Abarbanel, Saul; and Don, Wai-Sun: *The Theoretical Accuracy of Runge-Kutta Time Discretizations for the Initial Boundary Value Problem: A Careful Study of the Boundary Error.* NASA CR-191561, ICASE Rep. No. 93-83, 1993.

53. Shapiro, Ralph: Linear Filtering. *Math. Comput.*, vol. 29, no. 132, Oct. 1975, pp. 1094–1097.

54. Eriksson, L.-E.: *Boundary Conditions for Artificial Dissipation Operators.* FFA TN 1984-53, Aeronaut. Res. Inst. Sweden, Oct. 1984.

55. Poinsot, T. J.; and Lele, S. K.: Boundary Conditions for Direct Simulations of Compressible Viscous Flows. *J. Comput. Phys.*, vol. 101, no. 1, July 1992, pp. 104–129.

56. Don, Wai-Sun; and Gottlieb, David: *Spectral Simulation of Unsteady Compressible Flow Past a Circular Cylinder.* NASA CR-182030, ICASE Rep. No. 90-29, 1990.

57. Abarbanel, Saul S.; Don, Wai Sun; Gottlieb, David; Rudy, David H.; and Townsend, James C.: Secondary Frequencies in the Wake of a Circular Cylinder With Vortex Shedding. *J. Fluid Mech.*, vol. 225, 1991, pp. 557–574.

58. Fornberg, Bengt: On a Fourier Method for the Integration of Hyperbolic Equations. *SIAM J. Numer. Anal.*, vol. 12, no. 4, Sept. 1975, pp. 509–528.

59. Beckers, J. M.: Analytical Linear Numerical Stability Conditions for an Anisotropic Three-Dimensional Advection-Diffusion Equation. *SIAM J. Numer. Anal.*, vol. 29, no. 3, June 1992, pp. 701–713.

Definitions of Symbols Used in Tables

$A, B, \ldots$	coefficients in predictor-corrector stencils
$\alpha, \beta, \ldots, \Upsilon, a, b, \ldots$	coefficients in matrices $\mathbf{P}$ and $\mathbf{Q}$
$\lambda_{\mathbf{A}}, \lambda_{\mathbf{B}}, \lambda_{\mathbf{M}}$	CFL numbers for matrices $\mathbf{A}$, $\mathbf{B}$, and $\mathbf{M}$
$\lambda_{\max}$	maximum CFL number
ξ	wave number

Subscripts:

L	left
R	right

Table 1. Extended MacCormack Predictor-Corrector Stencils

Scheme	β	α	A	B	C	D	E	F	G	$\lambda_{\max}$
(2-2E)	0	0	$\frac{1}{2}$	$\frac{1}{2}$	0	0	0	0	-1	1.00
(2-4E)	0	0	$\frac{2}{3}$	0	$-\frac{1}{12}$	$\frac{1}{3}$	0	0	$-\frac{2}{3}$	0.72
(2-4T)	0	$\frac{1}{4}$	$\frac{3}{4}$	$\frac{\sqrt{3}}{4}$	0	0	0	0	$-\frac{\sqrt{3}}{2}$	0.57
(2-6E)	0	0	$\frac{3}{4}$	$\frac{1}{5}$	$-\frac{3}{20}$	$\frac{2}{7}$	$\frac{1}{60}$	$\frac{2}{7}$	$-\frac{54}{35}$	0.63
(2-6T)	0	$\frac{1}{3}$	$\frac{7}{9}$	$\frac{1}{3}$	$\frac{1}{36}$	$\frac{1}{45}$	0	0	$-\frac{32}{45}$	0.50
(2-6P)	$-\frac{1}{114}$	$\frac{17}{57}$	$\frac{15}{19}$	$\frac{5}{13}$	0	0	0	0	$-\frac{10}{13}$	0.48
(2-8T)	0	$\frac{3}{8}$	$\frac{25}{32}$	$\frac{1}{4}$	$\frac{1}{20}$	$-\frac{7}{9}$	$-\frac{1}{480}$	$-\frac{1}{2}$	$-\frac{37}{18}$	0.46
(2-8P)	$\frac{1}{36}$	$\frac{4}{9}$	$\frac{20}{27}$	$\frac{1}{10}$	$\frac{25}{216}$	$\frac{1}{4}$	0	0	$-\frac{7}{10}$	0.45

Table 2. Skewed Viscous Stencils

Scheme	d_L	c_L	b_L	a_L	Υ	a_R	b_R	c_R	d_R	e_R
First order forward	0	0	0	0	-1	1	0	0	0	0
Third order forward	0	0	0	$-\frac{1}{3}$	$-\frac{1}{2}$	1	$-\frac{1}{6}$	0	0	0
Fifth order forward	0	0	$\frac{1}{20}$	$-\frac{2}{4}$	$-\frac{1}{3}$	1	$-\frac{2}{8}$	$\frac{1}{30}$	0	0
Seventh order forward	0	$-\frac{1}{105}$	$\frac{1}{10}$	$-\frac{3}{5}$	$-\frac{1}{4}$	1	$-\frac{3}{10}$	$\frac{1}{15}$	$-\frac{1}{140}$	0
Ninth order forward	$\frac{1}{504}$	$-\frac{1}{42}$	$\frac{1}{7}$	$-\frac{4}{6}$	$-\frac{1}{5}$	1	$-\frac{4}{12}$	$\frac{2}{21}$	$-\frac{1}{56}$	$\frac{1}{630}$

Table 3. RKLW Predictor-Corrector Stencils

Scheme	β	α	A	B	C	D	E	F	G	$\lambda_{\max}$
(3-2E)	0	0	$\frac{1}{2}$	$\frac{1}{2}$	0	0	0	0	-1	1.59
(3-4E)	0	0	$\frac{2}{3}$	0	$-\frac{1}{12}$	$-\frac{2}{9}$	0	0	$\frac{4}{9}$	1.34
(3-4T)	0	$\frac{1}{4}$	$\frac{3}{4}$	$\frac{1}{5}$	0	0	0	0	$-\frac{2}{5}$	1.06
(3-6E)	0	0	$\frac{3}{4}$	$\frac{3}{5}$	$-\frac{3}{20}$	$-\frac{1}{5}$	$\frac{1}{60}$	$-\frac{1}{5}$	$-\frac{2}{5}$	1.15
(3-6T)	0	$\frac{1}{3}$	$\frac{7}{9}$	$\frac{4}{21}$	$\frac{1}{36}$	$-\frac{6}{11}$	0	0	$\frac{164}{231}$	.92
(3-6P)	$-\frac{1}{114}$	$\frac{17}{57}$	$\frac{15}{19}$	$\frac{1}{5}$	0	0	0	0	$-\frac{2}{5}$	.94
(3-8T)	0	$\frac{3}{8}$	$\frac{25}{32}$	$\frac{11}{20}$	$\frac{1}{20}$	$-\frac{3}{5}$	$-\frac{1}{480}$	$-\frac{11}{20}$	$\frac{6}{5}$	.83
(3-8P)	$\frac{1}{36}$	$\frac{4}{9}$	$\frac{20}{27}$	$\frac{2}{25}$	$\frac{25}{216}$	$-\frac{5}{13}$	0	0	$\frac{198}{325}$	.84
(3-10P)	$\frac{1}{20}$	$\frac{1}{2}$	$\frac{17}{24}$	$\frac{3}{5}$	$\frac{101}{600}$	$-\frac{4}{5}$	$\frac{1}{600}$	$-\frac{11}{20}$	$-\frac{3}{2}$	.76

Table 4. Fourth- and Third-Order Runge-Kutta Stencils

Accuracy									$\lambda_{\max}$	
Fourth order	Third order	β	α	a	b	c	d	e	Fourth order	Third order
(4-4E)	(3-4E)	0	0	$\frac{2}{3}$	$-\frac{1}{12}$	0	0	0	2.06	1.26
(4-4T)	(3-4T)	0	$\frac{1}{4}$	$\frac{3}{4}$	0	0	0	0	1.63	1.00
(4-6E)	(3-6E)	0	0	$\frac{3}{4}$	$-\frac{3}{20}$	$\frac{1}{60}$	0	0	1.78	1.09
(4-6T)	(3-6T)	0	$\frac{1}{3}$	$\frac{7}{9}$	$\frac{1}{36}$	0	0	0	1.42	0.87
(4-6P)	(3-6P)	$-\frac{1}{114}$	$\frac{17}{57}$	$\frac{15}{19}$	0	0	0	0	1.44	0.88
(4-8E)	(3-8E)	0	0	$\frac{4}{5}$	$-\frac{1}{5}$	$\frac{4}{105}$	$-\frac{1}{280}$	0	1.63	1.00
(4-8T)	(3-8T)	0	$\frac{3}{8}$	$\frac{25}{32}$	$\frac{1}{20}$	$-\frac{1}{480}$	0	0	1.32	0.81
(4-8P)	(3-8P)	$\frac{1}{36}$	$\frac{4}{9}$	$\frac{20}{27}$	$\frac{25}{216}$	0	0	0	1.28	0.78
(4-10E)	(3-10E)	0	0	$\frac{5}{6}$	$-\frac{5}{21}$	$\frac{5}{84}$	$-\frac{5}{504}$	$\frac{1}{1260}$	1.53	0.94
(4-10T)	(3-10T)	0	$\frac{2}{5}$	$\frac{39}{50}$	$\frac{1}{15}$	$-\frac{1}{210}$	$\frac{1}{4200}$	0	1.26	0.77
(4-10P)	(3-10P)	$\frac{1}{20}$	$\frac{1}{2}$	$\frac{17}{24}$	$\frac{101}{600}$	$\frac{1}{600}$	0	0	1.21	0.74

Table 5. Temporal Accuracy of (4-8P) Scheme on $U_t + U_x = 0$

CFL	$(7^4, 7^4, 7^4, 7^4\text{-}8\text{-}7^4, 7^4, 7^4, 7^4)$ $\log_{10} L_2$	Convergence rate
0.8	-5.282	
0.6	-5.896	4.91
0.4	-6.638	4.21
0.2	-7.854	4.04
0.1	-9.053	3.98
0.05	-9.399	1.15

Table 6. Spatial Accuracy of (4-8P) Scheme on $U_t + U_x = 0$

Grid	$(7^4, 7^4, 7^4, 7^4\text{-}8\text{-}7^4, 7^4, 7^4, 7^4)$ $\log_{10} L_2$	Convergence rate
41	-4.933	
51	-5.741	8.34
101	-8.388	8.79
151	-9.797	8.00
201	-10.606	6.48

Table 7. Temporal Accuracy of Third-Order Runge-Kutta and RKLW Schemes on $U_t + U_x = 0$

	RK		RKLW	
Grid	(3, 3-4-3, 3) $\log_{10} L_2$	Convergence rate	(3, 3-4-3, 3) $\log_{10} L_2$	Convergence rate
41	-2.512		-1.877	
51	-2.794	2.91	-2.121	2.60
101	-3.681	2.94	-2.913	2.62
201	-4.575	2.97	-3.672	2.53
251	-4.864	2.98	-3.910	2.43
501	-5.763	2.99	-4.612	2.33
1001	-6.665	2.99	-5.275	2.20
2001	-7.567	3.00	-5.911	2.11
4001	-8.469	3.00	-6.531	2.06
8001	-9.369	2.90	-7.143	2.03
16001	-10.099	2.42	-7.749	2.01

Table 8. Stability of Various Boundary Closures

Interior stencil		Scheme	$\max \Re(\lambda_{\mathbf{A}})$ $(n = 51)$	$\max \Re(\lambda_{\mathbf{A}})$ $(n = 201)$	$\max \Re(\lambda_{\mathbf{A}})$ $(n = 501)$
Order	Type				
Fourth	Explicit	(3,3-4-3,3)	-2.92×10^{-5}	-4.32×10^{-7}	-2.75×10^{-8}
Fourth	Tridiagonal	(3-4-3)	-2.66×10^{-5}	-3.88×10^{-7}	-2.45×10^{-8}
Sixth	Explicit	(3,3,4-6-4,3,3)	-4.41×10^{-5}	-6.33×10^{-7}	-3.99×10^{-8}
Sixth	Explicit	$(5^2, 5^2, 5\text{-}6\text{-}5, 5^2, 5^2)$	-1.01×10^{-3}	-1.17×10^{-5}	-7.07×10^{-7}
Sixth	Tridiagonal	(3,4-6-4,3)	-6.03×10^{-5}	-8.82×10^{-7}	-5.57×10^{-8}
Sixth	Tridiagonal	$(5^2, 5^2\text{-}6\text{-}5^2, 5^2)$	-1.24×10^{-3}	-1.56×10^{-6}	-9.60×10^{-8}
Sixth	Pentadiagonal	(3,4-6-4,3)	-5.57×10^{-5}	-8.14×10^{-7}	-5.14×10^{-8}
Sixth	Pentadiagonal	$(5^2, 5^2\text{-}6\text{-}5^2, 5^2)$	-3.30×10^{-4}	-5.08×10^{-5}	-6.48×10^{-6}
Eighth	Explicit	(3,3,4,4-8-4,4,3,3)	-1.22×10^{-5}	-1.55×10^{-7}	-9.56×10^{-9}
Eighth	Explicit	(3,3,4,6-8-6,4,3,3)	-2.18×10^{-5}	-2.92×10^{-7}	-1.81×10^{-8}
Eighth	Explicit	$(7^4, 7^4, 7^4, 7^4\text{-}8\text{-}7^4, 7^4, 7^4, 7^4)$	-8.50×10^{-4}	-9.11×10^{-6}	-5.43×10^{-7}
Eighth	Tridiagonal	(3,4,4-8-4,4,3)	-5.48×10^{-5}	-7.72×10^{-7}	-4.84×10^{-8}
Eighth	Tridiagonal	(3,4,6-8-6,4,3)	-7.58×10^{-5}	-1.01×10^{-6}	-6.95×10^{-8}
Eighth	Tridiagonal	$(7^4, 7^4, 7^4, 7^4\text{-}8\text{-}7^4, 7^4, 7^4, 7^4)$	-1.74×10^{-3}	-1.89×10^{-5}	-1.13×10^{-6}
Eighth	Pentadiagonal	(3,4-8-4,3)	-8.15×10^{-5}	-1.20×10^{-6}	-7.55×10^{-8}
Eighth	Pentadiagonal	$(7^4, 7^4, 7^4, 7^4\text{-}8\text{-}7^4, 7^4, 7^4, 7^4)$	-4.56×10^{-3}	-1.67×10^{-4}	-8.48×10^{-6}
Tenth	Explicit	(3,3,4,4,4-10-4,4,4,3,3)	-2.04×10^{-6}	-2.28×10^{-8}	-1.30×10^{-9}
Tenth	Explicit	(3,3,4,6,8-10-8,6,4,3,3)	-9.58×10^{-6}	-1.19×10^{-7}	-7.32×10^{-8}
Tenth	Tridiagonal	(3,4,4,4-10-4,4,4,3)	-1.89×10^{-5}	-2.38×10^{-7}	-1.46×10^{-8}
Tenth	Tridiagonal	(3,4,6,8-10-8,6,4,3)	-5.78×10^{-5}	-8.09×10^{-7}	-5.06×10^{-8}
Tenth	Pentadiagonal	(3,4,4-10-4,4,3)	-4.51×10^{-5}	-6.13×10^{-7}	-3.82×10^{-8}
Tenth	Pentadiagonal	(3,4,8-10-8,4,3)	-8.10×10^{-5}	-1.17×10^{-6}	-7.37×10^{-8}

Table 9. Stability of Boundary Closures for Dissipative Schemes for $\mathbf{M} = \frac{1}{2}\left(\mathbf{A}^{+}\mathbf{A}_{v}^{-} + \mathbf{A}^{-}\mathbf{A}_{v}^{+}\right)$

$[0.001 \equiv 1.00(-3)]$

Stencil (a)	Boundary closure scheme	Error max $\Re(\lambda_{\mathbf{M}})$ ($n = 51$) (a)	Error max $\Re(\lambda_{\mathbf{M}})$ ($n = 201$) (a)	Error max $\Re(\lambda_{\mathbf{M}})$ ($n = 501$) (a)
(2-2E) [(3-2E)]	(1-2-1)	$-3.94(-3)$ [$-3.94(-3)$]	$-2.47(-4)$ [$-2.47(-4)$]	$-3.95(-5)$ [$-3.95(-5)$]
(2-4E) [(3-4E)]	(3,3-4-3,3)	$-3.94(-3)$ [$-3.94(-3)$]	$-2.47(-4)$ [$-2.47(-4)$]	$-3.95(-5)$ [$-3.95(-5)$]
(2-4T) [(3-4T)]	(3-4-3)	$-3.94(-3)$ [$-3.94(-3)$]	$-2.47(-4)$ [$-2.47(-4)$]	$-3.95(-5)$ [$-3.95(-5)$]
(2-6E) [(3-6E)]	(3,3,4-6-4,3,3)	$-3.94(-3)$ [$-3.94(-3)$]	$-2.47(-4)$ [$-2.47(-4)$]	$-3.95(-5)$ [$-3.95(-5)$]
(2-6E) [(3-6E)]	($5^2, 5^2$, 5-6-5,$5^2, 5^2$)	$-3.94(-3)$ [$-3.94(-3)$]	$-2.47(-4)$ [$-2.47(-4)$]	$-3.95(-5)$ [$-3.95(-5)$]
(2-6T) [(3-6T)]	(3,4-6-4,3)	$-3.77(-3)$ [$-3.76(-3)$]	$-2.44(-4)$ [$-2.44(-4)$]	$-3.93(-5)$ [$-3.93(-5)$]
(2-6T) [(3-6T)]	($5^2, 5^2$-6-$5^2, 5^2$)	$-2.93(-3)$ [$-2.93(-3)$]	$-2.27(-4)$ [$-2.27(-4)$]	$-3.81(-5)$ [$-3.81(-5)$]
(2-6P) [(3-6P)]	(3,4-6-4,3)	$+1.67(+2)$ [$+2.49(+2)$]	$+1.72(+2)$ [$+2.56(+2)$]	$+2.12(+2)$ [$+3.29(+2)$]
(2-6P) [(3-6P)]	($5^2, 5^2$-6-$5^2, 5^2$)	$+6.65(+2)$ [$+7.40(+2)$]	$+6.65(+2)$ [$+7.40(+2)$]	$+6.65(+2)$ [$+7.40(+2)$]
(2-8T) [(3-8T)]	(3,4,4-8-4,4,3)	$+2.61(+0)$ [$-9.42(-3)$]	$+2.73(+0)$ [$-4.66(-3)$]	$+2.74(+0)$ [$-4.38(-3)$]
(2-8T) [(3-8T)]	(3,4,6-8-6,4,3)	$+2.61(+0)$ [$-9.42(-3)$]	$+2.73(+0)$ [$-4.66(-3)$]	$+2.74(+0)$ [$-4.38(-3)$]
(2-8T) [(3-8T)]	($7^4, 7^4, 7^4, 7^4$-8-$7^4, 7^4, 7^4, 7^4$)	$+1.09(+1)$ [$+1.06(+1)$]	$+1.09(+1)$ [$+1.06(+1)$]	$+1.09(+1)$ [$+1.06(+1)$]
(2-8P) [(3-8P)]	(3,4-8-4,3)	$-3.70(-3)$ [$-3.73(-3)$]	$-2.43(-4)$ [$-2.43(-4)$]	$-3.92(-5)$ [$-3.92(-5)$]
(2-8P) [(3-8P)]	($7^4, 7^4, 7^4, 7^4$-8-$7^4, 7^4, 7^4, 7^4$)	$+1.68(+2)$ [$+1.68(+2)$]	$+1.68(+2)$ [$+1.68(+2)$]	$+1.68(+2)$ [$+1.68(+2)$]
[(3-10P)]	(3, 4, 4-10-4, 4, 3)	[$-3.95(-3)$]	[$-2.47(-4)$]	[$-3.95(-5)$]
[(3-10P)]	(3,4,6-10-6,4,3)	[$-3.95(-3)$]	[$-2.47(-4)$]	[$-3.95(-5)$]
[(3-10P)]	(3,4,8-10-8,4,3)	[$-3.95(-3)$]	[$-2.47(-4)$]	[$-3.95(-5)$]

[a]Brackets indicate values from scheme 2; other values are from scheme 1.

Table 10. Interior Filter Stencil, Second-Order Accurate Stencils for $\left[-\frac{\partial^{2n} f}{\partial x^{2n}}\right]$

$\left[\frac{\partial^{2n} f}{\partial x^{2n}}\right]$	Υ	a	b	c	d	e	f	g	h	i	j
$\left[\frac{\partial^{2} f}{\partial x^{2}}\right]$	+2	−1	0	0	0	0	0	0	0	0	0
$\left[\frac{\partial^{4} f}{\partial x^{4}}\right]$	−6	+4	−1	0	0	0	0	0	0	0	0
$\left[\frac{\partial^{6} f}{\partial x^{6}}\right]$	+20	−15	+6	−1	0	0	0	0	0	0	0
$\left[\frac{\partial^{8} f}{\partial x^{8}}\right]$	−70	+56	−28	+8	−1	0	0	0	0	0	0
$\left[\frac{\partial^{10} f}{\partial x^{10}}\right]$	+252	−210	+120	−45	+10	−1	0	0	0	0	0
$\left[\frac{\partial^{12} f}{\partial x^{12}}\right]$	−924	+792	−495	+220	−66	+12	−1	0	0	0	0
$\left[\frac{\partial^{14} f}{\partial x^{14}}\right]$	+3432	−3003	+2002	−1001	+364	−91	+14	−1	0	0	0
$\left[\frac{\partial^{16} f}{\partial x^{16}}\right]$	−12870	+11440	−8008	+4368	−1820	+560	−120	+16	−1	0	0
$\left[\frac{\partial^{18} f}{\partial x^{18}}\right]$	+48620	−43758	+31824	−18564	+8568	−3060	+816	−153	+18	−1	0
$\left[\frac{\partial^{20} f}{\partial x^{20}}\right]$	−184756	+167960	−125970	+77520	−38760	+15504	−4845	+1140	−190	+20	−1

Table 11. Truncation Error of First Derivative Operators

Accuracy	Explicit	Tridiagonal	Pentadiagonal	Heptadiagonal	Nonadiagonal
Fourth order	$-\frac{1}{30}\xi^5$	$-\frac{1}{180}\xi^5$			
Sixth order	$-\frac{1}{140}\xi^7$	$-\frac{1}{2100}\xi^7$	$-\frac{1}{1512}\xi^7$		
Eighth order	$-\frac{1}{630}\xi^9$	$-\frac{1}{17640}\xi^9$	$-\frac{1}{44100}\xi^9$	$-\frac{23}{226800}\xi^9$	
Tenth order	$-\frac{1}{2772}\xi^{11}$	$-\frac{1}{124740}\xi^{11}$	$-\frac{1}{582120}\xi^{11}$	$-\frac{1}{495000}\xi^{11}$	$-\frac{263}{14968800}\xi^{11}$

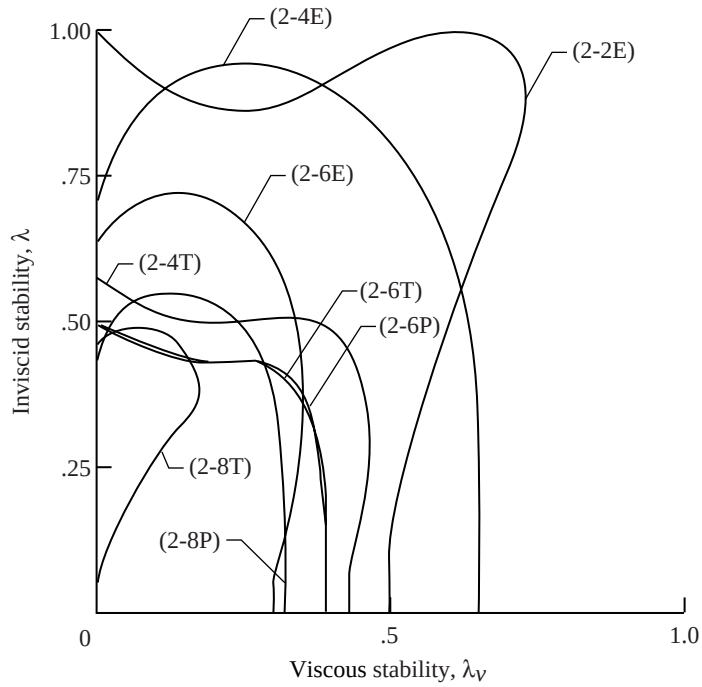

Figure 1. Stability limits of extended MacCormack schemes on one-dimensional convection-diffusion equation as function of inviscid CFL (λ) and viscous CFL (λ_v) numbers.

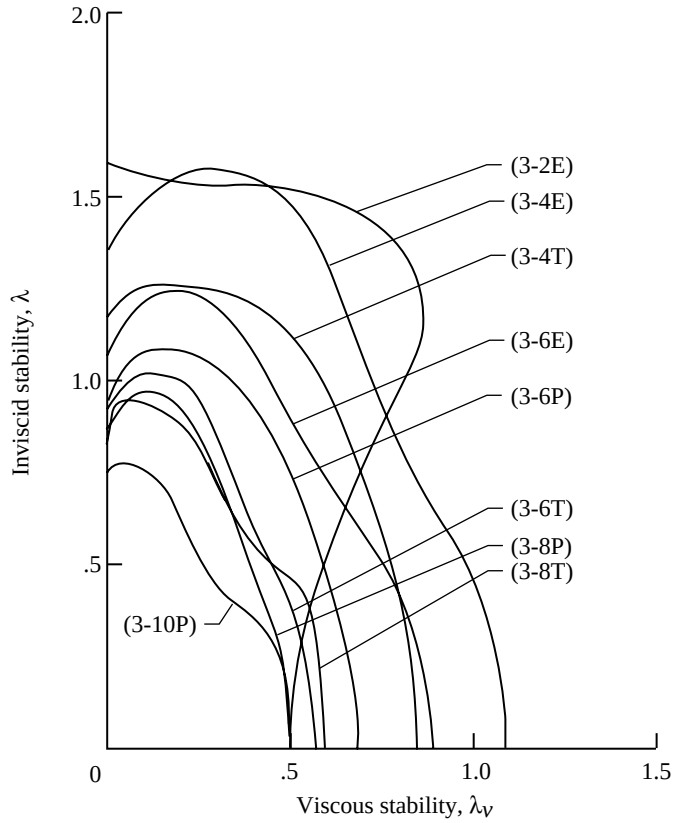

Figure 2. Stability limits of RKLW schemes on one-dimensional convection diffusion equation as function of inviscid CFL (λ) and viscous CFL (λ_v) numbers.

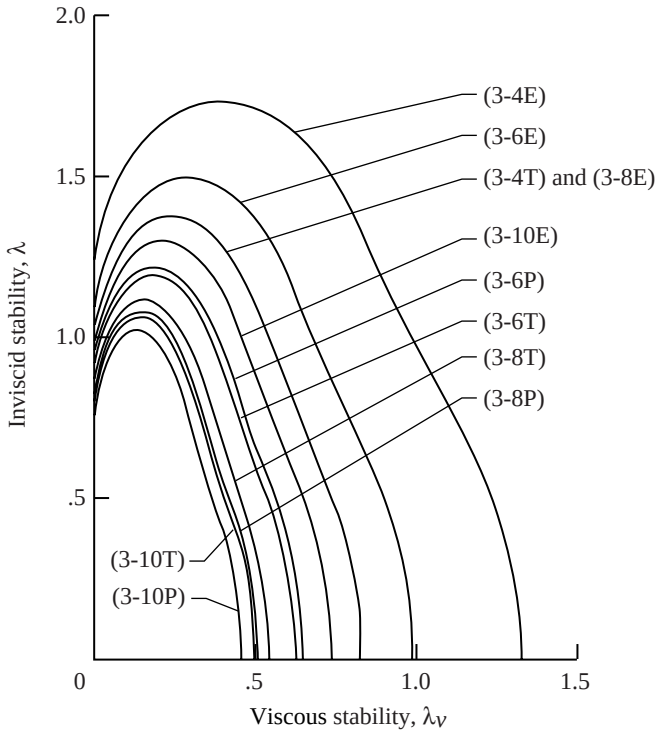

Figure 3. Stability limits of third-order Runge-Kutta schemes on one-dimensional convection-diffusion equation as function of inviscid CFL (λ) and viscous CFL (λ_v) numbers.

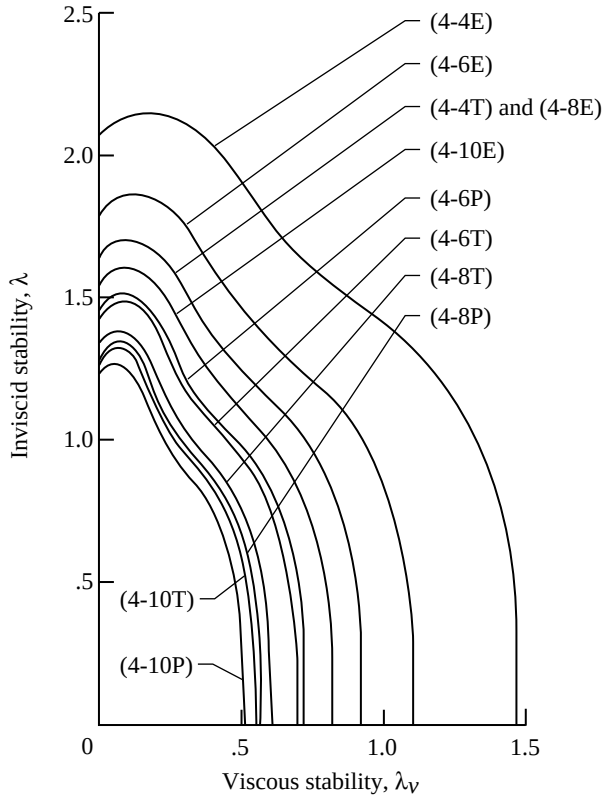

Figure 4. Stability limits of fourth-order Runge-Kutta schemes on one-dimensional convection-diffusion equation as function of inviscid CFL (λ) and viscous CFL (λ_v) numbers.

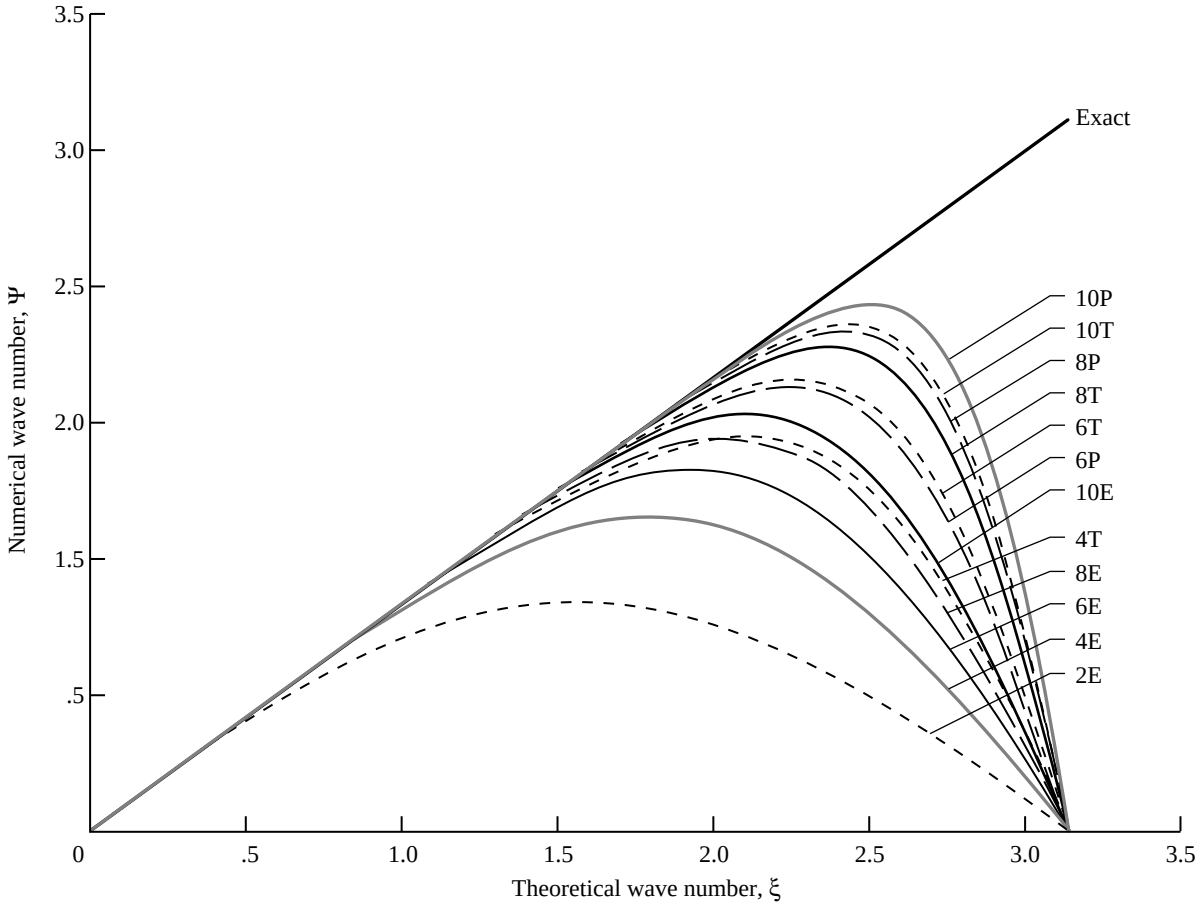

Figure 5. Various Fourier images of first-derivative spatial operator compared with exact Fourier derivative as function of wave number ξ.

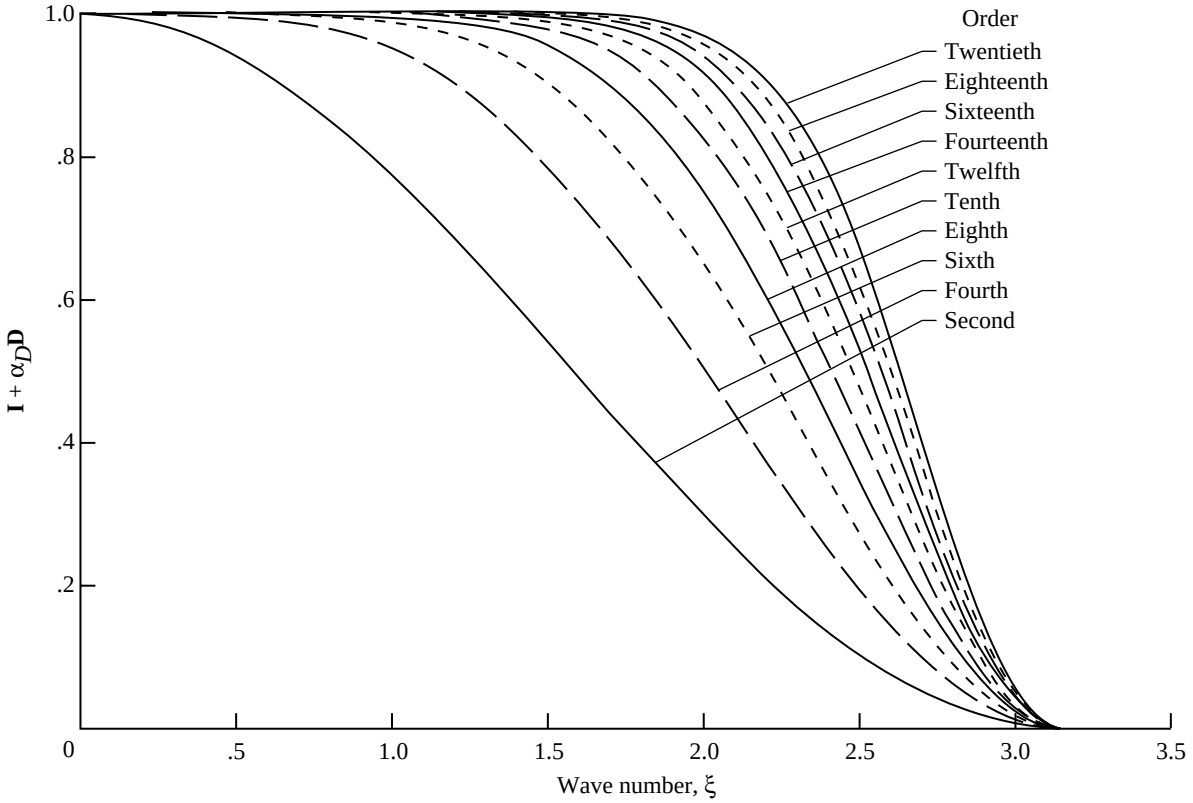

Figure 6. Filter functions of various orders in Fourier space as function of wave number ξ.

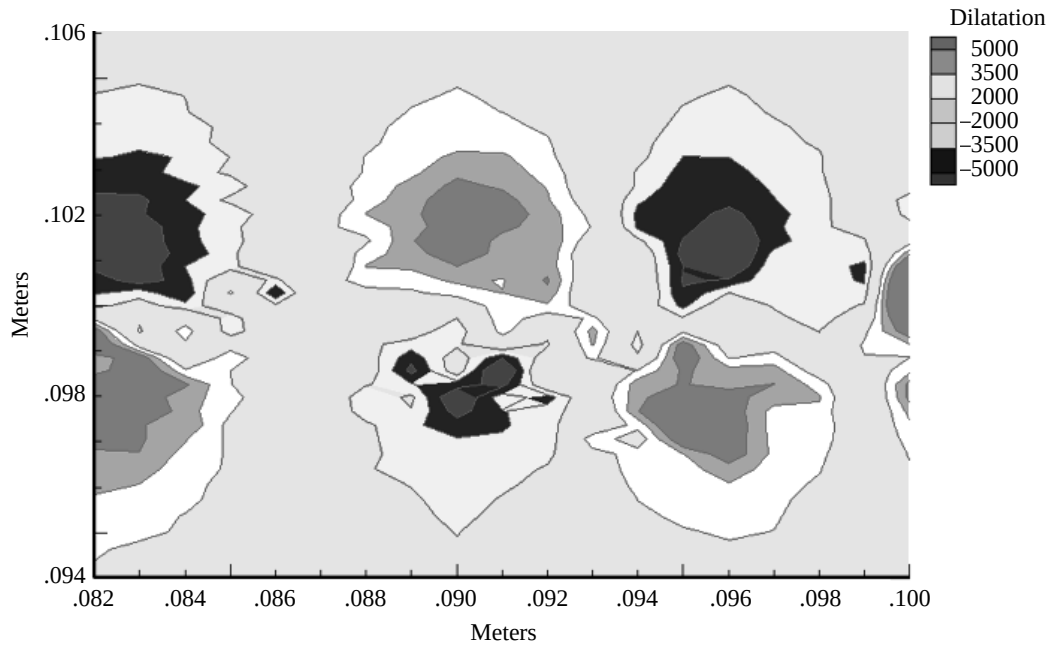

(a) Unfiltered (2-4T) scheme on 101 by 151 grid.

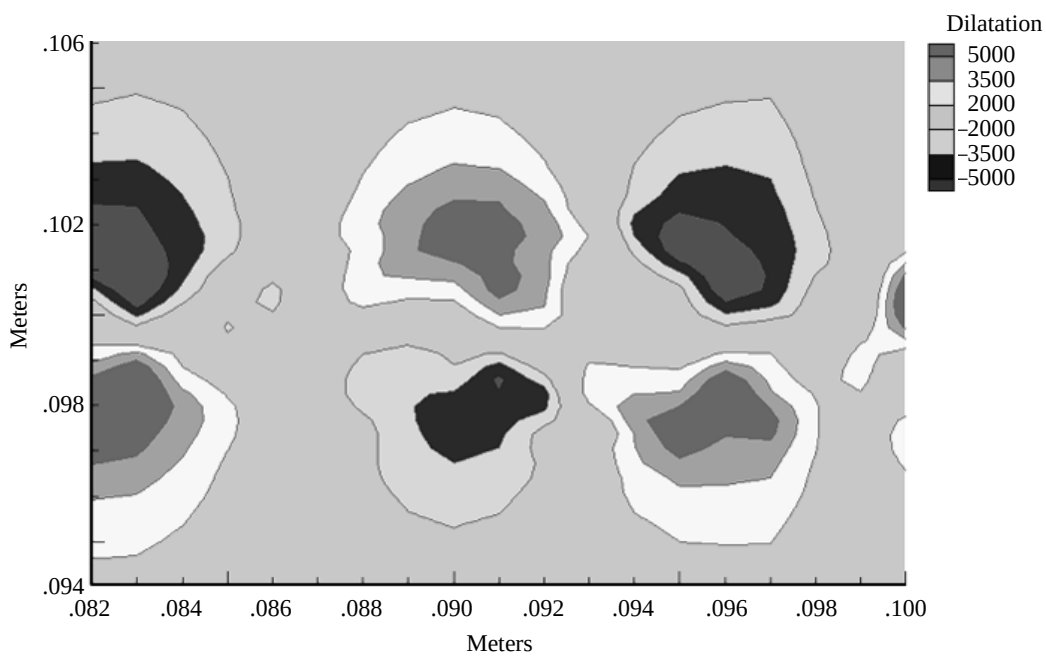

(b) Filtered (2-4T) scheme on 101 by 151 grid.

Figure 7. Dilatation field $\nabla \cdot \vec{u}$ in nitrogen-nitrogen compressible shear layer at $\mathrm{Ma}_c = 0.45$.

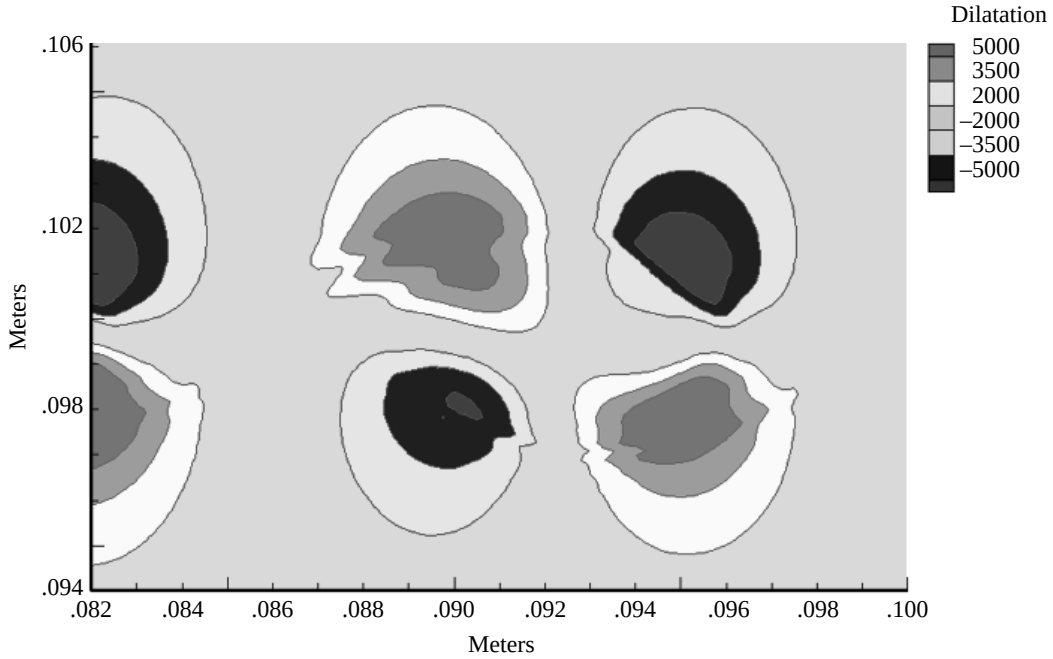

(c) Filtered (3-6T) RKLW scheme on 401 by 501 grid.

Figure 7. Concluded.

REPORT DOCUMENTATION PAGE

Form Approved
OMB No. 0704-0188

Public reporting burden for this collection of information is estimated to average 1 hour per response, including the time for reviewing instructions, searching existing data sources, gathering and maintaining the data needed, and completing and reviewing the collection of information. Send comments regarding this burden estimate or any other aspect of this collection of information, including suggestions for reducing this burden, to Washington Headquarters Services, Directorate for Information Operations and Reports, 1215 Jefferson Davis Highway, Suite 1204, Arlington, VA 22202-4302, and to the Office of Management and Budget, Paperwork Reduction Project (0704-0188), Washington, DC 20503.

1. AGENCY USE ONLY *(Leave blank)*

2. REPORT DATE
December 1997

3. REPORT TYPE AND DATES COVERED
Technical Paper

4. TITLE AND SUBTITLE
Comparison of Several Numerical Methods for Simulation of Compressible Shear Layers

5. FUNDING NUMBERS
WU 505-59-50-05

6. AUTHOR(S)
Christopher A. Kennedy and Mark H. Carpenter

7. PERFORMING ORGANIZATION NAME(S) AND ADDRESS(ES)
NASA Langley Research Center
Hampton, VA 23681-2199

8. PERFORMING ORGANIZATION REPORT NUMBER
L-17382

9. SPONSORING/MONITORING AGENCY NAME(S) AND ADDRESS(ES)
National Aeronautics and Space Administration
Washington, DC 20546-0001

10. SPONSORING/MONITORING AGENCY REPORT NUMBER
NASA TP-3484

11. SUPPLEMENTARY NOTES
Kennedy: University of California, San Diego, CA; Carpenter: Langley Research Center, Hampton, VA.

12a. DISTRIBUTION/AVAILABILITY STATEMENT
Unclassified–Unlimited
Subject Category 02
Availability: NASA CASI (301) 621-0390

12b. DISTRIBUTION CODE

13. ABSTRACT *(Maximum 200 words)*

An investigation is conducted on several numerical schemes for use in the computation of two-dimensional, spatially evolving, laminar variable-density compressible shear layers. Schemes with various temporal accuracies and arbitrary spatial accuracy for both inviscid and viscous terms are presented and analyzed. All integration schemes use explicit or compact finite-difference derivative operators. Three classes of schemes are considered: an extension of MacCormack's original second-order temporally accurate method, a new third-order variant of the schemes proposed by Rusanov and by Kutler, Lomax, and Warming (RKLW), and third- and fourth-order Runge-Kutta schemes. In each scheme, stability and formal accuracy are considered for the interior operators on the convection-diffusion equation $U_t + aU_x = \alpha U_{xx}$. Accuracy is also verified on the nonlinear problem, $U_t + F_x = 0$. Numerical treatments of various orders of accuracy are chosen and evaluated for asymptotic stability. Formally accurate boundary conditions are derived for several sixth- and eighth-order central-difference schemes. Damping of high wave-number data is accomplished with explicit filters of arbitrary order. Several schemes are used to compute variable-density compressible shear layers, where regions of large gradients exist.

14. SUBJECT TERMS
Numerical methods; Compressible flow; Binary mixtures; Numerical filters; Numerical accuracy; Runge-Kutta methods; Rusanov scheme; Finite difference methods; Shear layers; Mixing layers; Numerical stability; Compact finite difference; MacCormack's scheme; Kutler-Lomax-Warming scheme

15. NUMBER OF PAGES
62

16. PRICE CODE
A04

17. SECURITY CLASSIFICATION OF REPORT
Unclassified

18. SECURITY CLASSIFICATION OF THIS PAGE
Unclassified

19. SECURITY CLASSIFICATION OF ABSTRACT
Unclassified

20. LIMITATION OF ABSTRACT